

Accepted by ApJ on March 13, 2009.

## The End of the White Dwarf Cooling Sequence in M4: an efficient approach<sup>1</sup>

Luigi R. Bedin<sup>2</sup>, Maurizio Salaris<sup>3</sup>, Giampaolo Piotto<sup>4</sup>, Jay Anderson<sup>2</sup>, Ivan R. King<sup>5</sup>,  
Santi Cassisi<sup>6</sup>.

### ABSTRACT

We use 14 orbits of ACS observations to reach the end of the white-dwarf cooling sequence in the globular cluster M4. Our photometry and completeness tests show that the end is located at magnitude  $m_{F606W} = 28.5 \pm 0.1$ , which implies an age of  $11.6 \pm 0.6$  Gyr (internal errors only). This is consistent with the age from fits to the main sequence turn-off ( $12.0 \pm 1.4$  Gyr).

*Subject headings:* globular clusters: individual (NGC 6121) — white dwarfs

### 1. Introduction

Stellar evolution theory predicts that the remnants of the majority of stars with masses less than  $\sim 6\text{--}7M_{\odot}$  become white dwarfs (WDs) after their progenitors have lost a large

---

<sup>2</sup>Space Telescope Science Institute, 3800 San Martin Drive, Baltimore, MD 21218; [bedin;jayander]@stsci.edu

<sup>3</sup>Astrophysics Research Institute, Liverpool John Moores University, 12 Quays House, Birkenhead, CH41 1LD, UK; ms@astro.livjm.ac.uk

<sup>4</sup>Dipartimento di Astronomia, Università di Padova, Vicolo dell'Osservatorio 2, I-35122 Padova, Italy; giampaolo.piotto@unipd.it

<sup>5</sup>Department of Astronomy, University of Washington, Box 351580, Seattle, WA 98195-1580; king@astro.washington.edu

<sup>6</sup>INAF-Osservatorio Astronomico di Collurania, via M. Maggini, 64100 Teramo, Italy; cassisi@oa-teramo.inaf.it

<sup>1</sup>Based on observations with the NASA/ESA *Hubble Space Telescope*, obtained at the Space Telescope Science Institute, which is operated by AURA, Inc., under NASA contract NAS 5-26555, under GO-10146.

part of the envelope during the asymptotic giant branch (AGB) phase. Single-star evolution WDs are compact objects with masses between  $\sim 0.5$  and  $\sim 1.0 M_{\odot}$  (increasing slowly with increasing progenitor mass), comprising an electron-degenerate core made almost exclusively of carbon and oxygen, surrounded by a thin non-degenerate envelope ( $\sim 1\%$  in mass fraction). The temperature of the CO core is too low to ignite nuclear reactions, and electron degeneracy prevents any sizable contraction and associated temperature increase that would ignite carbon burning. The energy radiated from the WD photosphere is therefore the thermal energy of the non-degenerate ions contained in the core, and the WD evolution can be described as a cooling process (Mestel 1952).

WD evolutionary tracks in the color–magnitude diagram (CMD) are constant-radius sequences, which the stars follow as they fade with time to progressively fainter magnitudes and redder colors. Given that the older the WD the fainter its magnitude, the CMD of the WD population in a star cluster is expected to show a cut-off at a certain magnitude, because no WD has had time to become fainter than some limiting brightness (see, e.g., Winget et al. 1987).

From a theoretical point of view, one can predict a WD luminosity function (LF) for a single-burst stellar population of given age and metallicity by assuming an initial-mass-final-mass relation, and adopting an initial mass function (IMF), along with appropriate lifetimes for the progenitors (see, e.g., Richer et al. 2000).

All theoretical WD LFs for old stellar populations show a peak at the faint end, caused by the “piling up” at the bottom of the WD sequence, as the cooling rate slows down with decreasing effective temperature (and luminosity). The peak moves towards fainter luminosities as the cluster age increases, reflecting the increasing age. For simplicity, we will hereafter refer to this peak in the WD LF as the end of the WD CS. The location of the peak is therefore a measure of the age, and it is only mildly affected by the adopted IMF (see, e.g., Prada Moroni & Straniero 2007, Salaris 2009). In summary, it is possible to use the bottom of the WD cooling sequence (WD CS) to obtain an estimate of a cluster age, independent of the main-sequence turn-off (MS TO).

Theoretical predictions of the cut-off brightness as a function of age rely on accurate WD cooling models. Despite the apparent simplicity of the structure of WD stars, theoretical WD cooling times still show sizable uncertainties. These are related first of all to the chemical stratification of the core and mass fractions of the non-degenerate He and H layers. Additional uncertainties stem from the equation of state of the dense, cool ion gas, and the treatment of the crystallization process. The opacity of the envelope and the surface boundary conditions are also critical for the determination of the cooling rate of faint WDs older than a few Gyr, and are still subject to non-negligible uncertainties (Montgomery et

al. 1999, Salaris et al. 2000, Salaris 2009).

Thus far, age estimates that made use of the entire WD CS in old clusters (older than  $\sim 6$  Gyr) have been performed in only two cases: (1) the metal-poor globular cluster NGC 6397 (Richer et al. 2006, Anderson et al. 2008a), and (2) the old super-solar-metallicity open cluster NGC 6791 (Bedin et al. 2008a). In the case of NGC 6397 there seems to be a remarkable agreement between the age derived from WDs and the age derived from MS TO stars (Hansen et al. 2007). In the case of NGC 6791, by contrast, there seems to be a conflict with results from standard WD models (Bedin et al. 2005a, 2008a, 2008b).

M4 (NGC 6121) is the closest globular cluster to the Sun, but because of the large extinction along its line of sight, its apparent distance modulus ( $12.5 \pm 0.1$  mag in  $V$ , Richer et al. 2004) is comparable to that of NGC 6397 ( $12.6 \pm 0.1$  mag in  $V$ , Richer et al. 2008). The metallicity of M4 is intermediate between those of NGC 6397 and NGC 6791, making it particularly useful to test the ages derived from the WD CS.

The observation of the piling-up in the WD LF in M4 has been previously attempted with 123 orbits of *HST* using the Wide Field and Planetary Camera 2 (WFPC2), by Richer et al. (2002, GO-8679). Their photometry did indeed reach the sharp rise near the bottom of the WD LF, but failed to detect a clear drop beyond the peak (Richer et al. 2004, Hansen et al. 2002, 2004). These authors, however, were nevertheless able to obtain an age estimate from the cooling sequence by fitting theoretical models to the full two-dimensional WD color-magnitude diagram.

Thanks to the superior capabilities of the Advanced Camera for Surveys (ACS), and thanks also to our improved astrometric and photometric techniques, we can now push the limits somewhat deeper, and detect the drop of the WD LF, in just 14 *HST* orbits.

In Section 2 we give a brief description of the observations, reduction procedures, and calibrations. Section 3 describes the selection process of real stars and well-measured stars, and Section 4 deals with the completeness. In Section 5 we describe how we obtained proper motions, to produce a decontaminated (but incomplete) sample of the best-measured stars. In Section 6 we describe the observed CMD, and in Section 7 we present the WD LF. Section 8 presents a comparison between the observed CMD of M4 with that of NGC 6397, while Section 9 gives a detailed comparison of observations with theory. Finally, we give a summary of the results in Section 10.

## 2. Observations and Measurements

### 2.1. Observational Data

All data were taken with the Wide Field Channel (WFC) of the ACS. The observations in the F606W filter consist of 20 exposures of  $\sim 1200$  s (10 HST orbits in total) collected between July and August 2004 as part of the program GO-10146 (PI: Bedin). The observations were divided evenly between two different orientations so as to avoid putting PSF artifacts in the same relative positions with respect to real stars. The F775W filter data consist of 4 exposures of  $\sim 1200$  s (2 HST orbits) taken on 2005 June 27 as part of the same GO program, and 10 exposures of 360 s (2 HST orbits) obtained in 2002 July and 2003 June as part of the program GO-9578 (PI: Rhodes). GO-9578 had additional data from another HST orbit in 2003 January, but due to extremely high background this data was unusable for our purposes. Hereafter we will refer to all of these F606W and F775W exposures as the *deep* images. All images collected within GO-10146 were well dithered (according to the precepts of Anderson & King 2000), and in LOW SKY mode.

We also took a sample of short exposures to link the bright stars on the horizontal branch and near the main sequence turn-off to the same photometric system. At the beginning of each of our first five visits we took one short exposure, as follows: 0.5 s + 10 s in F606W, and 0.5 s +  $2 \times 10$  s in F775W. In addition, we used F606W archival material: 1 s +  $2 \times 25$  s +  $2 \times 30$  s (from program GO-10775, PI: Sarajedini).

### 2.2. Measurements and reduction

The photometry was carried out with the software tools described in great detail by Anderson et al. (2008b). Briefly, the method consists of a two-pass procedure. We start with a pair of “Library PSFs”, one for each filter, which had been constructed from other data sets. Each library PSF consists of a  $9 \times 10$  array of PSFs that represent how the ACS/WFC PSF varies across the detectors which we perturb slightly to fit each exposure as described in Anderson & King (2006, AK06). We then use this perturbed PSF to measure the fluxes and positions of the relatively isolated and relatively bright stars, using the code described in AK06. We then adopt the first deep F606W exposure as the reference frame, and find the 6-parameter linear transformation from the distortion-corrected frame of each exposure into this frame, using the positions of common stars. We also put the magnitudes into a common zero-point system based on the deepest F606W and F775W exposures.

In the second pass a sophisticated software routine analyzed simultaneously all the

individual exposures to find the brightest sources and to measure a single position and a F606W and an F775W flux for each of them. It then subtracts out the newly found sources from each exposure and iterates the finding procedures until no more significant objects are found. To qualify as found, an object has to be detected as a local maximum in at least 6 out of the 34 deep images. Many of these detections are simply coincident noise peaks, but we include them here to demonstrate how distinct the background-noise distribution is from our sources. Anderson et al. (2008b) describes how we manage to avoid including PSF artifacts in our star lists.

In addition to solving for positions and fluxes during the simultaneous-fitting process above, we also compute a very important image-shape diagnostic parameter for each source: RADXS. This is a measure of how much flux there is in the pixels just outside of the core, in excess of the prediction from the PSF. (We measure it using the pixels between  $r = 1.0$  and  $r = 2.5$ , and it is reported relative to the star’s total flux.) RADXS is positive if the object is broader than the PSF, and negative if it is sharper. This quantity is of great help in distinguishing between stars and galaxies whose images are nearly as sharp; the latter are especially numerous in the part of the CMD where the faint white dwarfs lie.

We compute a stacked image free of cosmic-rays and artifacts (see Fig. 1). We use this stack to construct two other important parameters for each detected object: these are the local sky background (SKY) and its r.m.s. deviation (rmsSKY), as defined in Bedin et al. (2008a).

Artificial-star (AS) tests are performed using the same procedure (Anderson et al. 2008b). For each AS, a position and a F606W magnitude are chosen in a random way; the F814W magnitude is then chosen so that the star’s color puts it on the ridge line of the WD sequence (drawn by eye). The AS is added into each exposure at the appropriate location, in the form of an appropriately scaled PSF with Poisson noise. The software routine then operates blindly, finding and measuring all the stars. We examine the resulting list of sources to determine whether the artificial star was recovered. The artificial stars are used not only as a measure of the completeness; they also serve, at a number of stages of the procedure, to help in developing and calibrating our criteria for the choice of valid stars.

For the analysis, we will follow closely the procedure recently applied with success to the study of the the WD CS of the open cluster NGC 6791 (Bedin et al. 2008a).

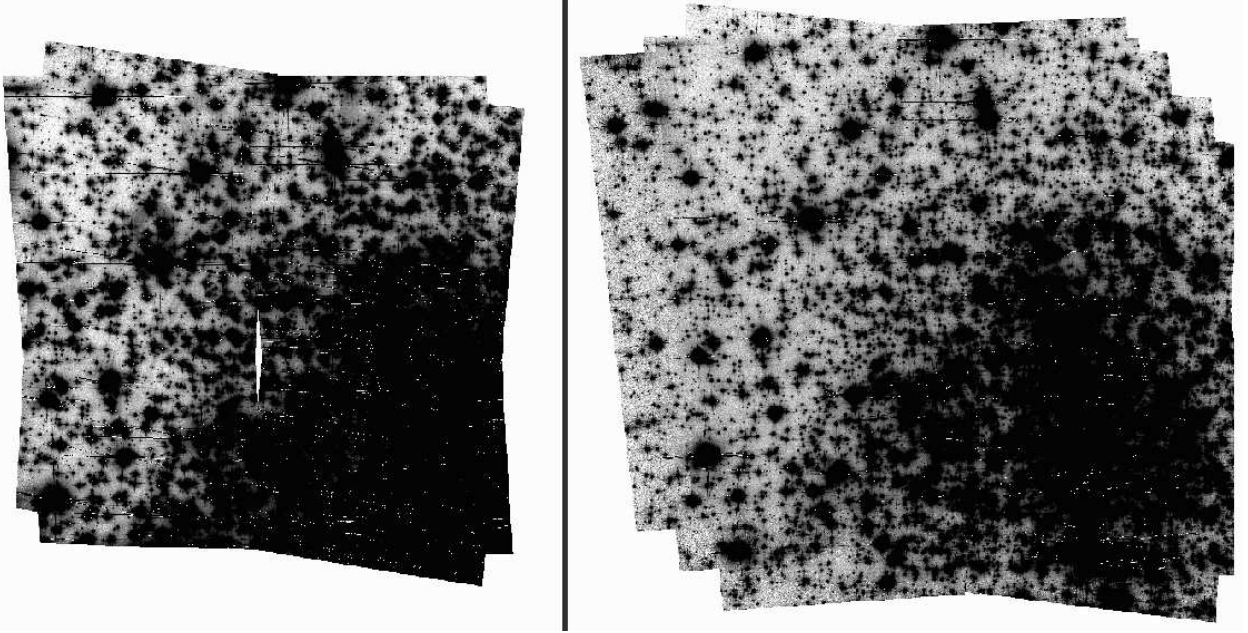


Fig. 1.— (*Left*) : Stacked image of deep exposures in filter F606W. (*Right*) : Stacked image of deep exposures in filter F775W. It is immediately clear that the region where we will be able to reach the faintest magnitudes will necessarily exclude the core of the cluster, where the halos of bright stars hide faint objects. The core regions instead provide good statistics for the fast evolutionary phases of the bright WDs. [Note that the brightest WDs are close to saturation in F606W].

### 2.3. Input-output corrections

Artificial-star tests allow us to assess precisely how many stars at each magnitude level were recovered by our algorithms and how well they were recovered. Figure 2 displays the difference between the inserted and recovered magnitudes of artificial stars for both filters. We divided the magnitude range covered by ASs into bins of half a magnitude, and estimated the median of the (output *minus* input) values for each of the stars within the bin (red dots). Magnitudes of the very faintest stars in the field are systematically overestimated by as much as  $\sim 0.2$  magnitude at  $m_{\text{F606W}} = 29$ .

These were used as fiducial points for our empirical correction. We applied to each star (artificial or real), in each magnitude independently, the correction obtained by a quadratic spline through the derived fiducial points. Figure 3 shows the result of the correction, which seems to do a good job overall. Hereafter, all the magnitudes will be corrected for this systematic photometric offset.

## 2.4. Photometric zero points

We calibrate the photometry to the WFC/ACS Vega-mag system following the procedure given in Bedin et al. (2005b), and using the encircled energy and the zero points given by Sirianni et al. (2005). Hereafter we will refer to these calibrated magnitudes with the symbols  $m_{\text{F606W}}$ , and  $m_{\text{F775W}}$ .

## 3. Selection of Stars

It is particularly important to identify galaxies and remove them from the star lists, because many of them fall in the part of the CMD where the faint end of the WD sequence lies. To distinguish these barely resolved objects from point sources, we use the shape parameter RADXS, which measures any excess flux just outside of the PSF core. Here the artificial stars are very instructive, since they show us how RADXS should behave with magnitude for true point sources. Panels *a)* and *a')* in Fig. 4 show us the trend of RADXS against F606W magnitude for artificial stars (bottom), and for objects that we have thus far considered to be real (top). It is clear that many of the objects that we have thus far included as stars are more extended than the artificial stars, which by definition have truly stellar profiles (because we made them that way). We use the distributions of the artificial stars to mark out boundaries in these diagrams that should retain nearly all the objects that are truly stars; they are indicated by the red lines, which were drawn in such a way as to include almost all of the recovered stars. They are repeated identically in the corresponding real-star panel. Note that the tail of objects on the right side in the AS panels is produced by star-star blends that our simultaneous-fitting routine was not able to separate into two components. These should certainly be eliminated from our photometry lists.

It is also clear that most of the objects found fainter than  $m_{\text{F606W}} \simeq 29.5$  are just peaks of the noise in the sky fluctuations. For reference, the lowest sky value in the typical 1200s F606W image is  $\sim 290$  DN, with a corresponding Poisson noise of  $\sim 17$  DN, which averaged on 20 deep F606W images becomes  $\sim 17/\sqrt{(20-1)} \simeq 4$  DN. Our PSF models tell us that the brightest pixel contains  $\sim 20\%$  of the light, so the total collected flux of the (PSF-fitted) peak of noise would be  $\sim 20$  DN, i.e. an instrumental magnitude of  $-2.5 \times \log_{10}(20) = -3.2$ . Since our zero point in F606W,  $ZP_{\text{F606W}}$ , is 34.04, our  $1\sigma$  level in filter F606W is  $m_{\text{F606W}} \simeq 30.8$ , the  $3\sigma$  level is at  $\simeq 29.6$ , and the  $5\sigma$  level at  $\simeq 29.0$ . Because of the many uncertainties in these calculations, in the following we will consider as *not significant* all the sources that our code measures to be fainter than  $m_{\text{F606W}} = 29$ . It is, however, instructive to show them in our plots during the selection procedures.

Our second image-quality parameter, rmsSKY, has a minor impact in the selection of stars, but it gives us invaluable information on how suitable the surroundings of each star are for good photometry. As the profiles of brighter stars have higher counts in their wings, and are consequently affected by greater Poisson noise, their rmsSKY also increases. This effect is clearly seen in panels *b)* and *b')* of Fig 4, which displays rmsSKY for real and artificial stars in a way exactly analogous to panels *a)* and *a')* for RADXS. Again, limit lines have been drawn by eye for the artificial stars, in a way that separates the stars found on flat background from those found in noisier areas. We will use rmsSKY again in Section 4, where it plays an even more important role.

Panels *c)* and *c')* of Fig. 4 show the CMD for real and artificial stars after applying our selection criteria on both RADXS and rmsSKY. The blue line shows the chosen fiducial line along which the ASs were added. We will hereafter consider as WDs of M4 all the stars that fall between the two red lines.

As an additional condition we selected only those ASs and real sources that fell in portions of the sky covered by all 20 deep images in F606W and at least 10 of the deep F775W images. These spatial selections are shown in panels *d)* and *d')* of Fig. 4 (in red we show the objects that do not pass these spatial criteria).

The WD CS that we find here for M4 is qualitatively consistent with the one exhibited by Hansen et al. (2004) based on their WFPC2 observations in a different field (see Fig. 4 in Richer et al. 2004), although it is difficult to compare the photometry in the F775W and F814W filters quantitatively.

#### 4. Completeness

Bedin et al. (2008a) make the point in their Section 4 that the main impediment to finding faint stars in *HST* images of globular clusters stems not from near-neighbor crowding, but from the presence of a few extremely bright giants. These giants have extended PSF halos that create a mottled background, making it hard to find faint stars in their vicinity. But in between these bright stars, it is easy to find and measure faint stars well. Whereas a given faint star may be found in only 25% of the field as a whole, if we search only in the flat areas between the bright giants, we may find it over 75% of the time.

We found in Bedin et al. (2008a) that our ability to find a given faint star depends most strongly on the flatness of the background upon which it is inserted. If we can determine what fraction of the image has a favorable background, we can then reliably assess what fraction of such stars could be found. This is the motivation for our construction of the



rmsSKY parameter: it allows us to search for stars only where they can be found easily. This has two advantages: when we find them, we measure them more accurately and, in addition, we tend to have far fewer false detections, since such detections are more likely in the less flat portions of the image.

Our completeness corrections for faint stars thus have two sources: an incompleteness due to the region not searched, and the incompleteness within the region searched. The net completeness is  $c$ , the fraction of stars recovered and it is the product of  $f_g$  (the fraction of the image that is searchable) and  $c_g$  (the fraction of the searchable region where the source was found). We define  $f_g$  for each brightness level of star to be the fraction of the the image where the background is flat enough to allow the artificial stars to be found. Both factors come from artificial-star tests, as shown in Bedin et al. (2008a).

The top right panel of Fig. 4 shows the completeness levels for our field. Figure 5 is the same as Fig. 4, but explicitly considers only the very best part (lowest crowding) of the whole field that we studied, the part of the image that is more than 2800 pixels ( $\simeq 140''$ ) from the estimated cluster center [marked with a  $\star$  in panels  $d$ ) and  $d'$ )]. We will explore the end of the WD CS only in the flatter parts of this sub-region of our field, but we will use the whole field to increase the star-count statistics in the fast evolutionary phases of the bright part of the WD CS.

In Fig. 5 the 50% level of “*overall completeness*”  $c$  is at  $m_{\text{F606W}} = 26.92$ , while that for the “*local completeness*”  $c_g$  it is at  $m_{\text{F606W}} = 28.95$ . Had we followed conventional rule of trusting only corrections with  $c > 50\%$ , we would have lost the faintest  $\sim 2$  magnitudes and thus missed the cutoff of the WD CS, which the real CMD and the artificial-star CMD clearly show we have reached. The top right panel of Figs. 4 and 5 also shows the fraction of the image area suitable for detection of faint sources (open circles). The product of this curve and  $c_g$  is of course the overall completeness  $c$ . Note how the fraction of usable field becomes about  $\sim 20\%$  at the faintest magnitudes in Fig. 4 (or about  $\sim 40\%$  in Fig. 5), which is crucial to the large correction applied to the observed WD LF (see Fig. 10).

## 5. Proper motions

Proper motions were measured with a technique similar to that described in detail in Bedin et al. (2003, 2006). As our first-epoch data (hereafter, epoch I) we used  $5 \times 360$  s F775W images collected on July 14, 2002 (GO-9578), while as epoch II we used  $4 \times 1200$  s exposures taken in June 27, 2005 (from our GO-10146), also in filter F775W to avoid the possibility of color-dependent systematic errors. To compute a proper motion for each star,

we first measured a mean position for the star in the reference frame at each epoch, using all the exposures within that epoch. The proper motion, then, is the difference between the second- and first-epoch positions, divided by the time baseline (2.95 yrs), and multiplied by the pixel scale (49.7 mas/pixel, van der Marel et al. 2007). The reference frame is aligned to have  $x$  and  $y$  parallel to RA and Dec, respectively, so the proper motions are in a properly aligned frame as well. The zero point of the motion is the cluster’s bulk motion, since the reference frame was defined by member stars.

Thanks to the very large proper motion of M4 with respect to both the field and background objects [about  $\sim 15$  mas yr $^{-1}$  (Bedin et al. 2003), i.e., almost a whole pixel in three years], as long as we were able to measure even a crude position in both epochs we were to get a good discriminant between field objects and cluster members (down to  $m_{\text{F606W}} \sim 29$ ).

Our first epoch is considerably shallower than the second epoch, which means that there is a good chance that the faintest stars will not be found in the first epoch and we will not get motions for them. If we were to require that all stars in our final sample have good proper motions, then our completeness would be severely limited by the first epoch. Nevertheless, even though we cannot do quantitative work with the proper motions, we can still use them in a qualitative way to illustrate the properties of the stars that we could measure.

The left panel of Fig. 6 shows as small dots all stars in panel c) of Fig. 5. Stars for which it was possible to estimate a proper motion are highlighted with open circles. In the second panel we show for this subsample of stars the magnitudes of the proper motions. Cluster stars have an internal dispersion of few km s $^{-1}$  (Peterson, Rees & Cudworth 1995), which at the distance of M4 corresponds to less than  $\sim 0.5$  mas yr $^{-1}$ . All field objects (Galactic disk in the foreground, and bulge stars, halo stars, and galaxies in the background) have a very different proper motion distribution, which clearly stands out from that of the members. Note the increasing size of random errors with decreasing S/N. In order to separate members from non-members we drew the red line by eye. Non-members, to the right of the red line, are marked with red crosses. In the third panel, using the same symbols, we show the vector-point diagrams (in mas yr $^{-1}$ ) for five different magnitude bins ( $m_{\text{F606W}} = 20\text{--}22$ ;  $22\text{--}24$ ;  $24\text{--}26$ ;  $26\text{--}28$ , and  $28\text{--}30$ ). The CMD that results from the cleaning criterion of the second panel is shown in the rightmost panel of the same figure.

## 6. The Color-Magnitude Diagram

In Fig. 7 we present the entire color-magnitude diagrams, for deep and short exposures, in both observational planes ( $m_{\text{F606W}} - m_{\text{F775W}}$ ,  $m_{\text{F606W}}$ ) and ( $m_{\text{F606W}} - m_{\text{F775W}}$ ,  $m_{\text{F775W}}$ ).

These CMDs span a factor of more than  $10^7$  in luminosity. All the main evolutionary sequences are very well defined, from the region of the hydrogen-burning limit up the MS through the turn-off, then almost to the tip of the red giant branch. The horizontal branch and white dwarf cooling sequence are also well represented.

This CMD, complete in all its relevant sequences, will be used in the following in order to measure the distance, reddening, and age of the cluster, from both the MS turn-off and the WD CS. A tricky part in producing the CMD of Fig. 7 was to link the  $\sim 1200$  s exposures to the relatively short exposures ( $\sim 10$  s) in filter F606W. To perform this task we used the calibrated catalog of M4 by Anderson et al. (2008b) to extend to brighter objects our calibrated deep photometry. Unsaturated stars that are common to the two independent calibrations show that they are in agreement to better than 0.01 magnitude. Our short exposures were zero-pointed consistently to the stars that are in common with the Anderson et al. (2008b) catalog. In filter F775W there were no difficulties in putting the photometry of the short exposures on the zero point of the deep calibrated exposures, as a number of stars are well exposed in both the several 360 s and the 1200 s frames.

The photometry obtained from short exposures comes from the first pass described in Section 2, wherein starlists are made from each individual exposure and these lists merged to yield the list of common stars. This yields different selection effects and therefore different completenesses than the comprehensive 2nd-pass procedure. But since these stars are all quite bright, it is safe to assume that they are nearly 100% complete and suffer very little neighbor contamination. We mark with a horizontal line the level below which photometry comes from deep exposures.

Even if the CMD is subject to incompleteness, the observed WD CS clearly piles up at  $m_{\text{F606W}} = 28.5 \pm 0.1$ , followed by an abrupt drop in a magnitude range where our completeness is still high. In the following Section we will give a more quantitative analysis of the completeness of the star counts in the lower part of the WD CS, and properly estimate the position of the WD LF peak.

In Figure 8 we show the two CMDs for just the proper-motion-decontaminated subsample obtained in Section 5, along with the photometric error ellipses along the WD fiducial line for six magnitude levels (at  $m_{\text{F606W}} = 24, 25, 26, 27, 28$ , and 29).

Although these CMDs are even more incomplete, and not amenable to reliable correction, they include the best astro-photometrically measured stars in our sample. To give a better idea of the objects we are dealing with, in Fig. 9 we show that two stars in the peak of the WD LF are clearly visible and measurable in both stacked images.

At the bottom of the WD CS there is some hint of a blue turn. However, the photometric

errors are too large to enable us to confirm its presence and measure its extension.

## 7. The White Dwarf Luminosity Function

Without a proper-motion elimination of field stars, the best we can do to derive a white dwarf luminosity function (WD LF) is what we did for NGC 6791 in Bedin et al. (2008a): we will use the RADXS parameter to remove as many galaxies and artifacts as we can, and delimit in color the region of the CMD in which we consider stars to be white dwarfs. For both of these tasks the artificial-star experiments prove to be extremely useful.

First, panel  $a'$ ) of Fig. 4 shows our treatment of the parameter RADXS. We used the results of our AS tests to draw our discriminating lines, in such a way as to include nearly all identified objects; we then applied those same selection criteria to the real stars, in panel  $a$ ).

We then chose our boundaries in the CMD, as indicated by the thin red lines in panel  $c'$ ) of Fig. 4. The boundaries were chosen so that only a marginal fraction of the artificial stars were lost, while the boundaries are set broadly enough to include all stars that might be white dwarfs of some sort—including WD binaries, and unusual types of WDs.

In the top panel of Fig. 10 we show the WD LF in our entire field as observed (thin-line histogram), and after correction for completeness (thick-line histogram). The vertical dashed line indicates the level of  $c_g=50\%$ , below which our completeness becomes unreliable. The bottom panel of the same figure shows the completeness-corrected LF for WDs within  $140''$  from the cluster center (labeled with INNER, in red), and for WDs outside that limit (OUTER, in blue). The shaded bins of the histograms indicate where the normalization to the entire field WD LF (ALL) was done. Note that  $c_g=50\%$ -level for OUTER reaches the faintest magnitudes, allowing us to follow the drop of the WD LF for almost two bins after the peak at  $m_{F606W} = 28.5$ .

The WD LF in the entire field (see top panel of Fig. 10) displays a clear increase in the number of objects fainter than  $m_{F606W} \sim 27.3$ , which corresponds to the location where  $T_{\text{eff}}$  decreases below  $\sim 5000$  K, assuming the distance modulus and WD isochrones described in Section 9. This feature is consistent with the luminosity function jump found by Hansen et al. (2004) at  $V > 27.4$  in their data, which they attribute to a drop in photospheric hydrogen opacity and a change in the boundary conditions of the cooling models.

The WDLF ends at a magnitude where our completeness is still reliable. In Table 1 we report the values of the entire WD LF. We must treat these numbers with care, however.

Table 1: Completeness-corrected white dwarf luminosity function (ALL). Note that the last point, at  $m_{\text{F606W}}=28.9$ , is beyond the limit of reliability for  $c_g$ .

$m_{\text{F606W}}$	$N_c$	$\sigma_{N_c}$	$m_{\text{F606W}}$	$N_c$	$\sigma_{N_c}$	$m_{\text{F606W}}$	$N_c$	$\sigma_{N_c}$
20.1	0.00	0.00	23.1	4.27	2.46	26.1	31.50	9.09
20.3	0.00	0.00	23.3	14.50	4.59	26.3	52.90	12.14
20.5	0.00	0.00	23.5	14.80	4.68	26.5	47.09	11.77
20.7	0.00	0.00	23.7	22.48	5.80	26.7	60.36	13.85
20.9	1.32	1.32	23.9	22.69	5.86	26.9	77.36	16.49
21.1	0.00	0.00	24.1	13.93	4.64	27.1	113.98	20.81
21.3	0.00	0.00	24.3	17.46	5.27	27.3	212.41	29.18
21.5	1.33	1.33	24.5	24.82	6.41	27.5	220.12	30.53
21.7	1.33	1.33	24.7	24.22	6.47	27.7	239.84	33.26
21.9	1.33	1.33	24.9	26.92	6.95	27.9	243.40	35.50
22.1	1.34	1.34	25.1	33.99	8.01	28.1	380.57	46.85
22.3	1.35	1.35	25.3	29.79	7.69	28.3	678.79	65.93
22.5	1.36	1.36	25.5	27.50	7.63	28.5	845.50	78.17
22.7	5.50	2.75	25.7	45.70	10.22	28.7	587.60	70.74
22.9	8.40	3.43	25.9	46.78	10.73	28.9	311.59	57.86

Because of energy equipartition the heavier WDs might have sunk into the center of the cluster, where we are considerably more incomplete. This might result in biases on the relative numbers of the WD LF.

Also, our numbers include no correction for point-like background galaxies that may have been included in our WD counts, though we expect this contamination to be small because of the care we took in eliminating non-stellar objects (see Section 3). We now turn to the question of contamination by background objects.

### 7.1. Contamination by background galaxies

Following the recipe and the motivations given by Bedin et al. (2008a) for a similar study of NGC 6791, in this section we use the Hubble Ultra Deep Field (HUDF; Beckwith et al. 2006) to assess whether the contamination by point-like background galaxies seriously

affects our WD CS, and/or WD LF.

We are thankful for two happy circumstances. First, part of the HUDF data-base is in the same photometric system ( $m_{F606W}$ ,  $m_{F775W}$ ) as our program, and second, we have already reduced and calibrated the HUDF with the same algorithms (Bedin et al. 2008a). The reduction of the HUDF subset of images presented in Bedin et al. (2008a) is complete down to the magnitudes of interest for this paper (once appropriate reddening is added). We note also that the HUDF, also observed with ACS/WFC, has the same area as our field.

In the left-hand panel of Fig. 11 we show the CMD of the objects in the HUDF that survived our selection criteria (in particular the selection on RADXS). A triangle indicates the region occupied by the bulk of point-like objects in the HUDF. The bottom edge of the triangle was chosen at an arbitrarily faint magnitude below which objects are no longer relevant to our M4 observations (see below).

If we assume that the distribution of the field objects in the HUDF is the same as that of the objects in our M4 field, we can apply the corresponding shifts in reddening ( $A_{F606W} - A_{F775W}$ ) and absorption ( $A_{F606W}$ ) and see if these objects overlap any of the location of the WS CS. In the right-hand panel of Fig. 11 we apply these shifts both to the HUDF objects and to the triangle, using the reddening law that applies to cool objects (4,000 K), from Bedin et al. (2005b, Table 3). We also indicate with a dashed line the position that the triangle would have if we had used the extinction law for hot objects (40,000 K), from Table 4 of the same work. As we can see, very few of the transformed HUDF objects fall between the two thin red lines that we used to select WDs in Section 3. In fact, this is a generous upper limit to the contamination, since, as we have explained in Sect. 4, we are using only a fraction of our M4 field to go deep. (Fig. 5). The black dots in right panel of Fig. 11 show the CMD presented in Fig. 5, while the blue circles are the subsample of proper motion selected stars shown in Fig. 6.

## 8. Comparison with NGC 6397 *HST* Observations

In the previous sections, we showed that with only 14 *HST* orbits we are able to reach the bottom of the WD CS. This result might seem surprising in view of the much larger number of orbits previously dedicated to the detection of the end of the WD CS in M4 (Richer et al. 2002, 2004, Hansen et al. 2002, 2004), and in NGC 6397 (Richer et al. 2006, 2008, Hansen et al. 2007, and Anderson et al. 2008a). As for M4, the papers based on the GO-8679 123 *HST* orbits used only WFPC2 images, and the superior quality of ACS/WFC is well known. As for the spectacular results of Richer and collaborators on NGC 6397,

they are indeed based on the 126 orbits of GO-10424. In addition, the F775W filter has a somewhat lower efficiency than the F814W filter used in GO-10424, and our field is in a more crowded region of the cluster. We believe that a major contributor is our overall strategy of data reduction and analysis. In fact, in this section we will show that the end of the WD CS in NGC 6397 can indeed be reached using just a subsample of 14 orbits from GO-10424. The purpose of this exercise is to validate the results that we will present in Section 9.

The subsample of GO-10424 data was extracted merely by taking the first images of that dataset, in alphabetic order, until we summed up a total observing time equivalent to our total exposure time in M4 in F606W ( $\sim 24,000$  s), and in F775W ( $\sim 8,500$  s). To reach these totals, we selected the first 34 images in F606W, and the first 12 F814W images of GO-10424, each with an average exposure time of  $\sim 710$  s ( $\pm 70$  s). (Note that to have the same total observing time used for M4, we need to use 15 orbits of GO-10424, instead of 14.)

In Figure 12 we compare our CMD of M4 (left) with the one of NGC 6397 that was obtained with an equal exposure time, and using the same procedures described in Sections 2 and 3 (middle panel). In the right-hand panel we show the CMD of NGC 6397 obtained from the entire GO-10424 data set (126 orbits), as obtained by Anderson et al. (2008a).

Note that: (1) we can reliably detect the end of the WD CS of NGC 6397 in this subset of 15 orbits of GO-10424; (2) the peak of the WD LF—what we call the end of the WD CS—of NGC 6397 is at  $m_{F606W} \sim 28.7$ , i.e., it is  $\sim 0.2$  magnitude fainter than the peak of the M4 WD LF; (3) we know that this is indeed the bottom of the WD CS, thanks to the much deeper CMD obtained using the entire data base; (4) the saturation level of deep exposures is at brighter magnitudes in NGC 6397 than in M4, because of the different exposure times ( $\sim 710$  s vs.  $\sim 1200$  s).

The M4 field is in the core of that cluster, while the NGC 6397 field from GO-10424 is in the outskirts, where the bright part of the CMD is poorly populated. In order to show the location of the NGC 6397 horizontal branch on the same CMD as the WDs, in the middle panel of Fig. 12 we plot the photometry from Anderson et al. (2008b). This was derived from the same combination of camera and filters used in GO-10424, but with shorter exposure times, and with the cluster center in the middle of the field of view (GO-10775, PI: Sarajedini).

## 9. Comparison with Theory

In this section we compare our observed CMD and LF with the predictions of stellar evolution and WD cooling models.

We have first fit the  $\alpha$ -enhanced ( $[\alpha/\text{Fe}] = 0.4$ ) isochrones and zero age Horizontal Branch (ZAHB) sequences by Pietrinferni et al. (2006—hereafter BaSTI isochrones) to the observed CMD, from the MS to the HB. This allows us to estimate the distance modulus and reddening that will be employed for the analysis of the WD cooling sequence. In addition, this fit provides the reference cluster age from the turn-off (TO) point, to be compared with the age derived from the WD LF. We have selected the BaSTI  $\alpha$ -enhanced isochrones and ZAHB with  $Z = 0.004$ , corresponding to  $[\text{Fe}/\text{H}] = -1.01$  (for  $[\alpha/\text{Fe}] = 0.4$ ), a value very close to the most recent spectroscopic estimate  $[\text{Fe}/\text{H}] = -1.07 \pm 0.01$  ( $[\alpha/\text{Fe}] = +0.39 \pm 0.05$ ) by Marino et al. (2008).

Before using these models to fit the cluster CMD we had to consider carefully two issues, related to the extinction along the line of sight to this cluster. The first point is that the extinction is high for M4 ( $A_V > 1$ ), and it also varies across the face of the cluster (see, e.g., Cudworth & Rees 1990, Liu & Janes 1990, Mochejska et al. 2002). This is due to the fact that the line of sight to M4 passes through the outer regions of the Scorpius-Ophiucus dark cloud complex.

It is well known that the ratio between the extinction in a given photometric band ( $A_\lambda$ ) and  $A_V$  depends on the flux distribution of the stellar source, and is in principle dependent on parameters like  $T_{\text{eff}}$ ,  $\log g$ , and chemical composition (see, e.g., Bedin et al. 2005b and Girardi et al. 2008 for discussions and data specific for the ACS photometric filters). So long as  $A_V$  is small, this effect is also small and a single value of  $A_\lambda/A_V$  can be safely applied along the whole isochrone. But the high value of  $A_V$  in the case of M4 makes it necessary to consider, in the fits to the observed CMD, the variation of  $A_\lambda/A_V$  along the isochrones. This effect is especially relevant in the F606W band, as shown by Fig. 2 of Girardi et al. (2008) and Tables 3 and 4 of Bedin et al. (2005b). With high values of  $A_V$  one also has to consider the so-called “Forbes” effect, discussed in detail by Girardi et al. (2008), i.e., the variation of the ratio  $A_\lambda/A_V$  for a given flux distribution, as the total extinction increases.

The second major issue is related to the value of the ratio  $R_V = A_V/E(B - V)$ , which affects the shape of the extinction curve. A number of investigations (see, e.g., Dixon & Longmore 1993, Ivans et al. 2001) have given indications that in the direction of M4  $R_V$  is higher than the standard  $R \sim 3.1\text{--}3.2$ , with values up to  $R_V \sim 4.2$  (Chini 1981). Here we assume  $R_V = 3.8$ , as in Hansen et al. (2004), consistent with the value obtained by Clayton & Cardelli (1998) for  $\sigma$  Sco, a star one degree away from M4 in the plane of the sky.

To include all these effects in our fits to the CMD of M4, we proceeded as follows. We first used the web interface at <http://stev.oapd.inaf.it/cgi-bin/cmd>, which implements the results by Girardi et al. (2008), to determine the extinctions in the F606W and F775W filters, covering the full range of  $T_{\text{eff}}$  of our isochrones and ZAHB, for  $Z = 0.004$ , and for varying



values of  $A_V$ . These extinctions are calculated assuming  $R_V = 3.1$  and the extinction law by Cardelli et al. (1989). We then included the effect of  $R_V = 3.8$  by multiplying these derived extinctions by a constant factor (very close to unity, however) that takes into account the variation of the ratios  $A_{F606W}/A_V$  and  $A_{F775W}/A_V$  (calculated at the central wavelength of the ACS filters) when changing  $R_V$  from 3.1 to 3.8, according to the Cardelli et al. (1989) extinction law. These final extinctions in the F606W and F775W bands were then applied to the BaSTI isochrones transformed to the ACS system using the bolometric corrections by Bedin et al. (2005b).

Figure 13 (top-right panel) displays the fits of the MS and the HB. The simultaneous match of the ZAHB to the lower envelope of the HB star distribution, and of the isochrones to the color of the unevolved MS and red giant branch (RGB), provide the apparent distance modulus  $(m-M)_{F606W} = 12.68$  and the extinction  $A_V = 1.2$ , which, for  $R_V = 3.8$ , corresponds to  $E(B - V) = 0.32$ . This value is consistent with the mean  $E(B - V) = 0.33 \pm 0.01$  determined for M4 by Ivans et al. (2001). Ages of 11, 12, and 13 Gyr are displayed. They roughly cover the full vertical extension of the observed SGB and match the bluest point along the observed MS, hence provide an estimate of the age range allowed by the isochrone-fitting procedure. The paucity of stars observed in our field along the HB phase makes it difficult to define unambiguously the observed ZAHB level; we estimated that this adds an uncertainty of  $\pm 0.10$  mag to the distance modulus obtained from ZAHB fitting. A  $\pm 0.10$  mag variation of the distance modulus implies an age uncertainty of  $\sim 1$  Gyr at these old ages, which added in quadrature to the uncertainty at fixed distance gives a final age estimate  $t = 12.0 \pm 1.4$  Gyr from the isochrone fitting.

The top-left panel of Fig. 13 shows the fit to the WD cooling sequence. We have employed the same distance, extinction, and ages listed above. WD isochrones for DA objects have been computed using the Salaris et al. (2000) WD tracks, the same bolometric corrections to the ACS system as in Bedin et al. (2005a), progenitor lifetimes from BaSTI, and a default initial-final mass relationship (IFMR):

$$M_{\text{WD}} = 0.54 M_{\odot} \exp [0.095(M_{\text{MS}} - M_{\text{TO}})]$$

where  $M_{\text{WD}}$  is the WD mass,  $M_{\text{MS}}$  its progenitor mass along the MS, and  $M_{\text{TO}}$  is the value of the stellar mass evolving at the TO point for the given cluster age. This relationship has the mathematical form of the IFMR used by Wood (1992) and is essentially the same as the one adopted in the Hansen et al. (2004) analysis, although our constant  $0.54 M_{\odot}$ —fixed considering the  $M_{\text{WD}}$  obtained from the synthetic AGB treatment by Cordier et al. (2007), for  $M_{\text{TO}}$  values in the relevant age range— is slightly different from the value of  $0.55 M_{\odot}$  adopted by Hansen et al. (2004). As for the extinction corrections, we used the Girardi et al. (2008) results as described above, but we had to employ MS stars covering the same  $T_{\text{eff}}$

values spanned by our cooling sequences, since the Girardi et al. (2008) calculations do not include WD models.

The bright part of the WD cooling sequence, down to  $m_{\text{F606W}} \sim 27$ , appears to be reproduced very well by the models. Some systematic color shifts appear at fainter magnitudes. These should not be interpreted in terms of a mismatch between the colors of the faint WD models and the observations, but as large errors in filter F775W. Our photometry is considerably more solid in filter F606W (for which we have 20 well-dithered exposures of 1200s each) than in filter F775W. This is due to the heterogeneous (and limited) material used for this red filter, which result in larger errors. For these reasons we will consider the luminosity functions only in filter F606W. [Note that this prevents us from clearly detecting color-features at the end of the WD CS.] We note, however, that Kowalski (2007) shows in his Figure 2 two  $0.6M_{\odot}$  WDs in the (F606W,F814W) plane employing model atmospheres calculated with and without the Ly- $\alpha$  far red wing opacity contribution (see also Kowalski & Saumon, 2006). The effect is important only for the cooler WDs. Our coolest WD temperatures are around 4000 K. At this  $T_{\text{eff}}$ , from Kowalski’s figure one can see that F606W must vary by definitely less than 0.1 mag, an amount smaller than the bin size of the LF and much smaller than the typical color error at these luminosities. The effect on the age from the LF is negligible. Kowalski estimates a difference of 0.5 Gyr on NGC 6397 WD ages, but he makes use of a fit of the location of the track on the CMD, not of the LF, as in our method.

The F606W magnitude of the termination of the observed WD sequence corresponds to age between 11 and 12 Gyr. We also display the location of a 12 Gyr isochrone for He-atmosphere WDs (type DB). These DB models have been calculated as described in Salaris et al. (2001), with the additional input that the boundary conditions for  $T_{\text{eff}}$  below 12,000 K are from the model atmospheres by Bergeron (1995). The mass fraction of the He-envelope is  $M_{\text{He}} = 10^{-3.5}M_{\text{WD}}$ , the same value assumed in the Hansen (1999) models. Bolometric corrections to the ACS system are from the same source employed in Bedin et al. (2005a), but for a pure-He atmosphere. We used the same IFMR employed to calculate the DA isochrones. The termination of the DB isochrone is located at much fainter magnitudes than the DA case, due to faster cooling times at low luminosities, and cannot be reached by the present data.

The lower panel of Fig. 13 displays a comparison between the observed LF in F606W (bin width of 0.2 mag) and the theoretical counterparts. Our primary aim here is to study the consistency between the age estimated from the cooling sequence — which is estimated from the magnitude level of the peak at the bottom of the WD sequence — and the TO age of this cluster. With our reference IFMR we computed theoretical LFs at fixed age, by

varying the exponent of the progenitor mass function, assumed to be a power law  $m^{-x}$ , the percentage of DB objects, and the percentage of unresolved WD binary systems (see Bedin et al. 2008b for a description of how to compute the WD LF, allowing for unresolved binary systems). The position of the peak caused by the termination of the DA cooling sequence is unaffected by these parameters. What is changed is the height of the peak compared to the level of the bright part of the LF, and the details of the overall shape of the LF. For example, the binary systems affect the shape of the LF mainly at the magnitude bins centered around  $m_{\text{F606W}} = 27.7$  and  $27.9$ , whereas the value of the exponent  $x$  and the DB fraction affect the height of the peak compared to the level of the LF at brighter magnitudes. In fact, there is a certain degree of degeneracy between the ratio of DB/DA objects and the exponent of the mass function. The effect of a mild increase of  $x$  (i.e., a more top-heavy mass function) on the overall shape of the LF can be counterbalanced by an increase of the fraction of DB objects.

Assuming a DB fraction of 30%, a typical value for the DB/DA ratio in the disk population (Tremblay & Bergeron 2008), and normalizing the theoretical LF to the observed number of objects between  $m_{\text{F606W}} = 25$  and  $26.5$ , the observed star counts are best reproduced by a progenitor mass function with  $x = -0.95$  (a value much higher than the standard Salpeter  $x = -2.35$  and in remarkable agreement with what was obtained by Bedin et al. 2001,  $x = -1$ ). A 5% fraction of binary WD+WD systems improves the fit right above (in brightness) the faint-end peak of the WD LF, and seems to be supported by both observational (Sommariva et al. 2008), and theoretical works (Heggie & Giersz 2008). Theoretical LFs for these choices of parameters and  $(m - M)_{\text{F606W}} = 12.68$  are displayed in Fig. 13, for the same three ages of 11, 12, and 13 Gyr as in the TO fits, plus a best-fit WD age of 11.6 Gyr, which has a  $\pm 0.6$  Gyr internal (only) error, due to the fit of the magnitude of the peak of the LF, and the uncertainty in our derived distance modulus.

## 10. Summary and discussion

Using only 14 *HST* orbits, we have been able to measure the location of the peak at the bottom of the WD CS in the globular cluster M4. This peak is located at magnitude  $m_{\text{F606W}} = 28.5 \pm 0.1$ .

We also obtained proper motions for a subsample of our stars and demonstrate that most of the objects along the observed WD CS are not foreground or background stars in the Galactic field. We also used a subset of the HUDF to demonstrate that our WD CS and WD LF are not appreciably contaminated by unresolved point-like background galaxies, which our proper motions cannot disentangle from members, because they are too faint to

be reliably found in our first epoch.

We have produced in a consistent photometric system a CMD which spans more than 18 magnitudes, going from the the bottom of the WD CS almost to the tip of the RGB. The CMD from the MS to the horizontal branch stage has been employed to determine the distance modulus, extinction, and MS turn-off age from isochrone fitting. A comparison of the observed WD LF with results from theoretical models provided an independent age determination. The age inferred from the WD LF is  $11.6 \pm 0.6$  Gyr, in good (internal) agreement with the age from fitting the main sequence turn-off ( $12.0 \pm 1.4$  Gyr). The error bars take into account only errors intrinsic to our methods and to the observations, not uncertainties in the adopted theoretical models. A detailed analysis of the absolute uncertainties in present-day WD models is beyond the purpose of this work, and will be performed in a separate paper (Salaris et al., in preparation). Salaris (2009) provides a rough estimate of the order of  $\pm 2$  Gyr, that takes into account current uncertainties on the CO stratification, envelope composition and thickness, IFMR and model input physics.

We note that both our turn-off and WD ages are consistent with the best-fit WD age of 12.1 Gyr derived for M4 by Hansen et al. (2004) employing different data, models, and methods. However, Hansen et al. (2004) age determination is based on an estimate of distance modulus and extinction obtained from the main-sequence-fitting to a ground-based fiducial main sequence, as described in Richer et al. (1997). This distance estimate makes use of pre-Hipparcos parallaxes for a set of field subdwarfs. The apparent distance modulus they obtain in  $V$  is 0.17 mag shorter than our estimate, and their extinction  $A_V$  is 0.12 mag higher than our result. In addition to the different pass-bands ( $V$  instead of  $m_{F606W}$ ) and methods, the well-documented reddening variations across the cluster may explain the different extinction estimates (assuming  $R_V = 3.8$ , a difference in  $A_V$  of 0.12 mag corresponds to a difference in reddening of  $E(B - V) \simeq 0.03$  between the two fields, consistent with the variation of the reddening detected in M4). The Hansen et al. (2004) lower extinction implies a true distance modulus shorter by  $\approx 0.3$  mag, when compared to our result. It is difficult to fully understand the reasons for this discrepancy. We can simply mention some inferences from the literature. First of all, main-sequence-fitting distances to globular clusters that make use of Hipparcos parallaxes of field subdwarfs tend to be systematically larger than pre-Hipparcos results (see, e.g., Gratton et al. 1997, Carretta et al. 2000). Also, post-Hipparcos main-sequence-fitting distances to globular clusters are systematically larger by 0.2-0.3 magnitudes compared to distances obtained from Baade-Wesslink (BW) methods applied to clusters' RR Lyraes (Gratton et al. 1997), whereas the result adopted by Hansen et al. (2004) appears to be consistent with BW analyses of M4 RR Lyraes. Overall, our longer distance to M4 seems to be consistent with the globular cluster distance scale set by the Hipparcos parallaxes of field subdwarfs. Our longer distance modulus can also at least partially explain why Hansen

et al. obtained a WD age of  $\sim 14 - 16$  Gyr with their method and the Salaris et al. (2000) cooling models, whereas we obtain a much lower age with the same set of models. Differences in the method for the WD age estimate may also play a relevant role in explaining this age discrepancy, as well as the fact that in our analysis we have accounted for the effect of the change of the  $A_\lambda/A_V$  ratio as a function of both the stellar flux distribution and of  $A_V$  itself, an effect not included in Hansen et al. study.

To demonstrate the robustness of our reduction strategy, we applied our techniques to a subset of the ACS/WFC GO-10424 images of the Galactic globular cluster NGC 6397, which we constructed to have the same total amount of exposure time for each filter as our M4 program. Although conditions might not be identical to those of M4 (different crowding, different red filter: F814W instead of F775W), we were able to locate the peak of the WD LF in NGC 6397 also, and found it at the same magnitude obtained from the entire 126-orbit data set (Anderson et al. 2008a), at  $m_{F606W} = 28.7 \pm 0.1$ .

It remains to be understood why the observed WD LF peak in NGC 6397 is  $\sim 0.2$  magnitude fainter than in M4. This, of course, can be due to the effect of different apparent distance moduli and/or cluster ages. De Angeli et al. (2005) determined the relative MS turn-off age for these two clusters, finding that M4 is  $\sim 10\%$  younger than NGC 6397. For the M4 age derived in this paper, this implies that NGC 6397 is  $\sim 1$  Gyr older. Such an age difference corresponds to a WD LF peak fainter by  $\sim 0.2$  mag, as observed. Therefore, if turn-off and WD relative ages between these two clusters are consistent, the apparent distance moduli have to be approximately the same. According to the results presented in Table 3 of Richer et al. (2008), NGC 6397 would have an apparent distance modulus in  $V \sim 0.1$  mag larger than the estimate by Hansen et al. (2004, see also Richer et al. 2004, Table 1) for M4. Allowing for this different distance modulus, the WD LF peak implies a NGC 6397 age about 0.5 Gyr older than M4, still in reasonable agreement with the turn-off relative ages. We note, however, that the difference in the apparent distance moduli for the two clusters is of about the same size as its uncertainties. A detailed comparative analysis between M4 and NGC 6397, determining distances, reddening, TO and WD ages in a homogeneous way will be also presented in the follow-up paper (Salaris et al., in preparation).

We thank the anonymous referee for the careful reading of the manuscript, and for the many useful comments. J.A. and I.R.K. acknowledge support from STScI grant GO-10146. G.P. acknowledges financial contribution from contract ASI-INAF I/016/07/0.

## REFERENCES

- Anderson, J., & King, I. R. 2000, *PASP*, 112, 1360
- Anderson, J., & King, I. R. 2006, PSFs, Photometry, and Astrometry for the ACS/WFC (Instrum. Sci. Rep. ACS 2006-01; Baltimore: STScI)
- Anderson, J., et al. 2008a, *AJ*, 135, 2114
- Anderson, J., et al. 2008b, *AJ*, 135, 2055
- Beckwith et al. 2006, *AJ*, 132, 1729
- Bedin, L. R., Anderson, King, I. R., & J. Piotto, G. 2001 *ApJ*, 560, L75
- Bedin, L. R., Piotto, G., King, I. R., & Anderson, J. 2003 *AJ*, 126, 247
- Bedin, L. R., Salaris, M., Piotto, G., King, I. R., Anderson, J., Cassisi, S., & Momany, Y. 2005a, *ApJ*, 624, L45
- Bedin, L. R., Cassisi, S., Castelli, F., Piotto, G., Anderson, J., Salaris, M., Momany, Y., & Pietrinferni, A. 2005b, *MNRAS*, 357, 1038
- Bedin, L. R., Piotto, G., Carraro, G., King, I. R., & Anderson, J. 2006, *A&A*, 460, L27
- Bedin, L. R., King, I. R., Anderson, J., Piotto, G. Salaris, M., Cassisi, S. & Serenelli, A. 2008a, *ApJ*, 678, 1279
- Bedin, L. R., Salaris, M., Piotto, G. Cassisi, S., Milone, A. P., Anderson, J., & King, I. R. 2008b, *ApJ*, 679, L29
- Bergeron, P., Saumon, D., & Wesemael, F. 1995 *ApJ*, 443, 764
- Cardelli, J. A., Clayton G. C., & Mathis, J. S. 1989, *ApJ*, 345, 245
- Carretta, E., Gratton, R.G., Clementini, G. & Fusi Pecci, F. 2000, *ApJ*, 533, 215
- Chini, R. 1981, *A&A*, 99, 346
- Clayton, G. C. & Cardelli, J. A. 1988, *AJ*, 96, 695
- Cordier, D., Pietrinferni, A., Cassisi, S. & Salaris, M. 2007, *AJ*, 133, 468
- Cudworth, K. M. & Rees R., 1990, *AJ*, 99, 1491
- De Angeli, F. et al. 2005, *AJ*, 130, 116

- Dixon, R. I. & Longmore, A. J. 1993, MNRAS, 265, 395
- Girardi, L. et al. 2008, PASP, 120, 583
- Gratton, R.G., Fusi Pecci, F., Carretta, E., Clementini, G., Corsi, C. E. & Lattanzi, M. 1997, ApJ, 491, 749
- Heggie, D. C. & Giersz, M. 2008, MNRAS, 389, 1858
- Hansen, B. M. S. 1999, ApJ, 520, 680
- Hansen, B. M. S. et al. 2002, ApJ, 574, L155
- Hansen, B. M. S. et al. 2004, ApJS, 155, 551
- Hansen, B. M. S. et al. 2007, ApJ, 671, 380
- Ivans, I. I. et al. 2001, RevMexAA (Serie de Conferencias), 10, 217
- Kowalski, P. M. & Saumon, D. 2006, ApJ, 651, 137
- Kowalski, P. M. 2007, A&A, 474, 491
- Liu, T. & Janes, K. A. 1990, ApJ, 360, 561
- Marino, A. F. Villanova, S., Piotto, G., Milone, A. P., Momany, Y., Bedin, L. R., & Medling, A. M. 2008, A&A, 490, 625
- Mestel, L. 1952, MNRAS, 112, 583
- Mochejska, B. J., Kaluzny, J., Thompson, I. & Pych, W. 2002, AJ, 124, 1486
- Montgomery, M. H., Klumpe, E. W., Winget, D. E., & Wood, M. A 1999, ApJ, 525, 482
- Pietrinferni, A., Cassisi, S., Salaris, M., & Castelli, F. 2006, ApJ, 642, 797
- Peterson, R. C., Rees, R. F. & Cudworth, K. M. 1995, ApJ, 443, 124
- Prada Moroni, P. G., & Straniero, O. 2007, A&A, 466, 1043
- Richer, H. B. et al. 1997, ApJ, 484, 741
- Richer, H. B. et al. 2000, ApJ, 529, 318
- Richer, H. B. et al. 2002, ApJ, 574, 151
- Richer, H. B. et al. 2004, AJ, 127, 2904

- Richer, H. B. et al. 2006, *Science*, 313, 936
- Richer, H. B. et al. 2008, *AJ*, 135, 2141
- Salaris, M. 2009, in proceedings of IAU Symposium 258: The Ages of Stars, Cambridge University Press, in press
- Salaris, M., García-Berro, E., Hernanz, M., Isern, J., & Saumon, D. *ApJ*, 2000, 544, 1036
- Salaris, M., García-Berro, E., Isern, J. & Torres, S. 2001, *A&A*, 371, 921
- Sirianni, M., et al. 2005, *PASP*, 117, 1049
- Sommariva, V., Piotto, G., Rejkuba, M., Bedin, L. R., Heggie, D. C., Mathieu, R. D., Villanova, S. *A&A*, 493, 947
- Tremblay, P. E. & Bergeron, P. 2008, *ApJ*, 672, 1144
- van der Marel et al. 2007 (Instrum. Sci. Rep. ACS 2007-07; Baltimore: STScI)
- Winget, D. E. et al. 1987, *ApJ*, 315, 77
- Wood, M.A. 1992 *ApJ*, 386, 539





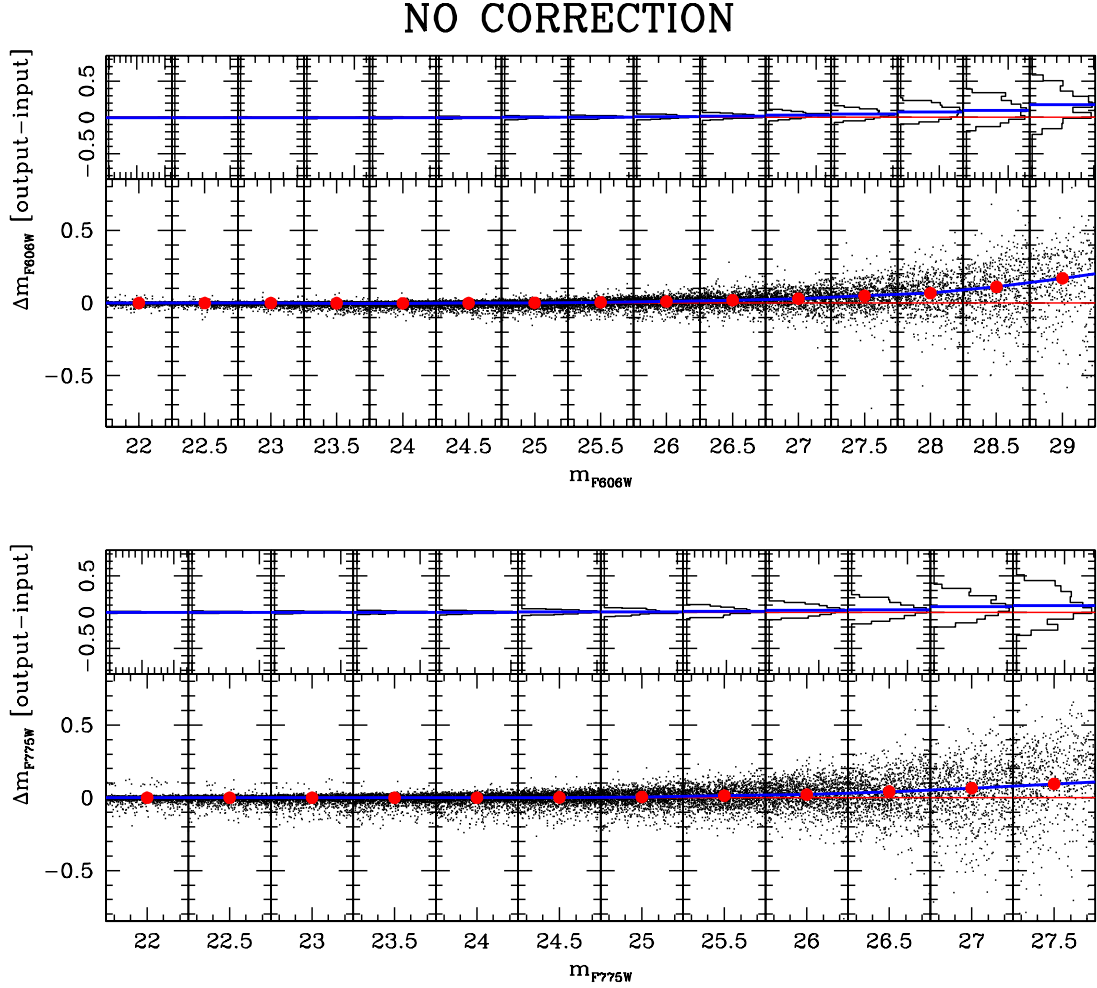


Fig. 2.— Difference between inserted and recovered AS magnitudes, for each filter separately (top panel F606W, bottom panel F775W). The lower part of each panel shows data points, while the upper part gives histograms of the same data. In the upper parts the red lines indicate the position of a null difference, while the blue lines are the observed median in the corresponding magnitude interval. In the lower parts the red horizontal lines indicate again the position of a null difference, while the blue lines now are the splines through the median values obtained in each magnitude interval (red dots).

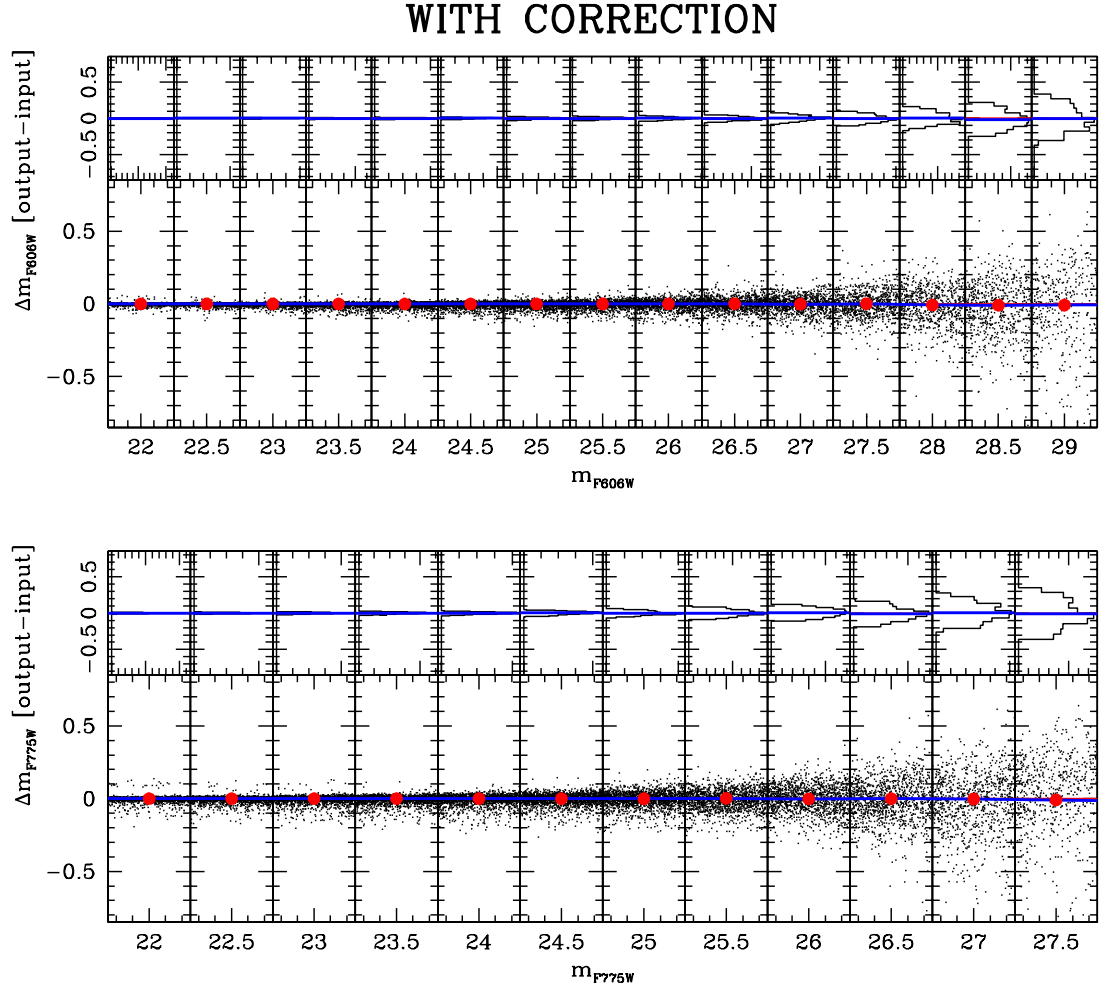


Fig. 3.— Difference between inserted and recovered AS magnitudes after the photometric-offset correction was applied.

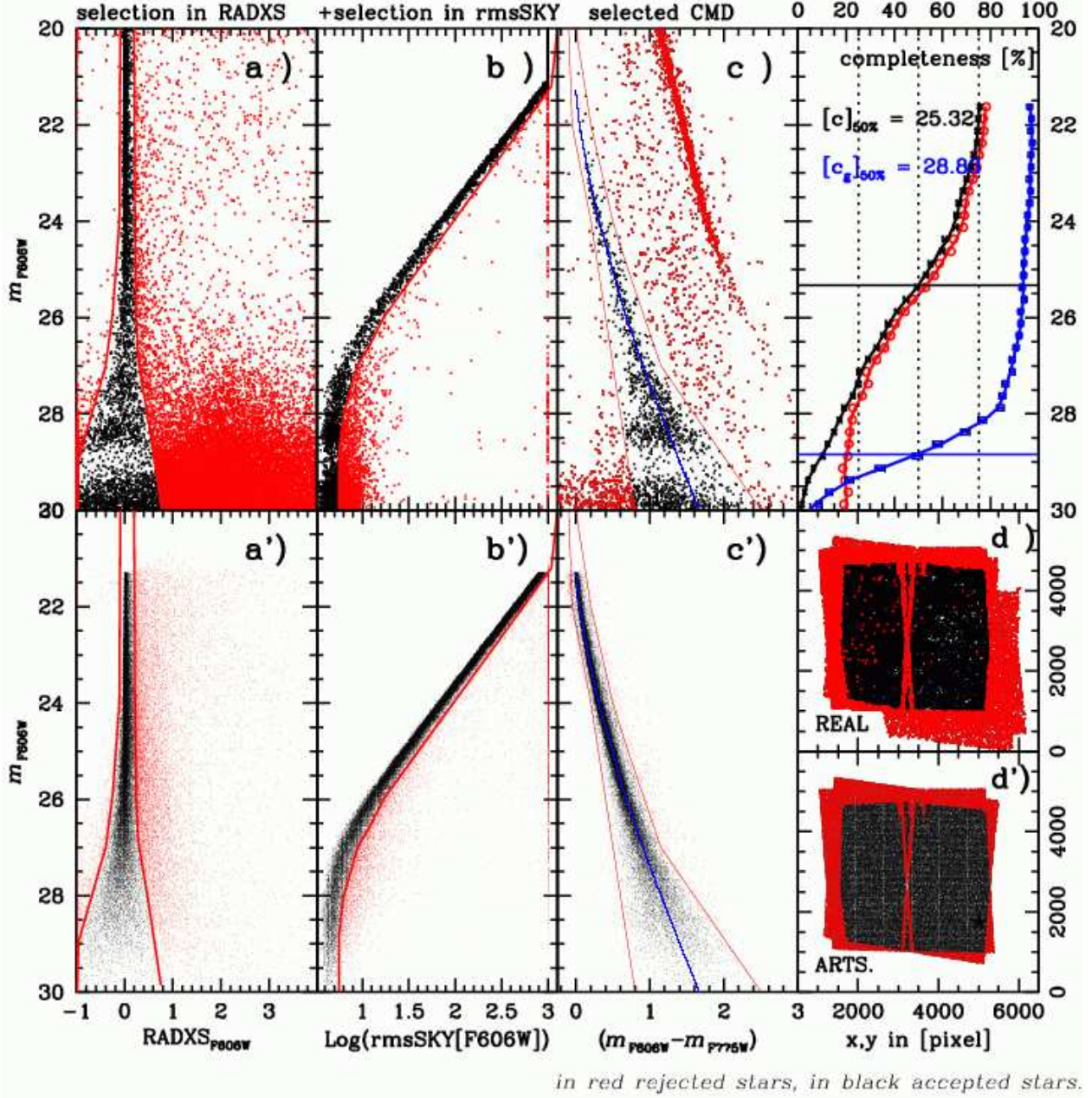


Fig. 4.— *Panels a), a')*: The parameter RADXS as a function of magnitude in filter F606W, for real and AS. Detections between the two red lines are considered to be real stars. *Panels b), b')*: The parameter rmsSKY as a function of magnitude after selection in RADXS, for real and AS. *Panels c), c')*: the CMD for the selected real and AS detections. Note that everything below  $m_{F606W} \simeq 29.5$  is essentially noise (see text). All the objects between the two thin red lines are considered WDs. *Panels d), d')*: spatial distribution of the real and AS detections. In black, objects that fell in all 20 F606W deep images and in at least 10 of the F775W deep images. *Top right*: The black crosses show the conventional completeness  $c$ , while the blue squares are the low-rmsSKY completeness  $c_g$  that is defined in the text. The red circles indicate the fraction of the image area  $f_g$  where the bumpiness of the of the sky offers no impediment to finding a star, at each magnitude. Note that at the faintest magnitudes about  $\sim 20\%$  of the observed field is useful for determination of the WD LF.



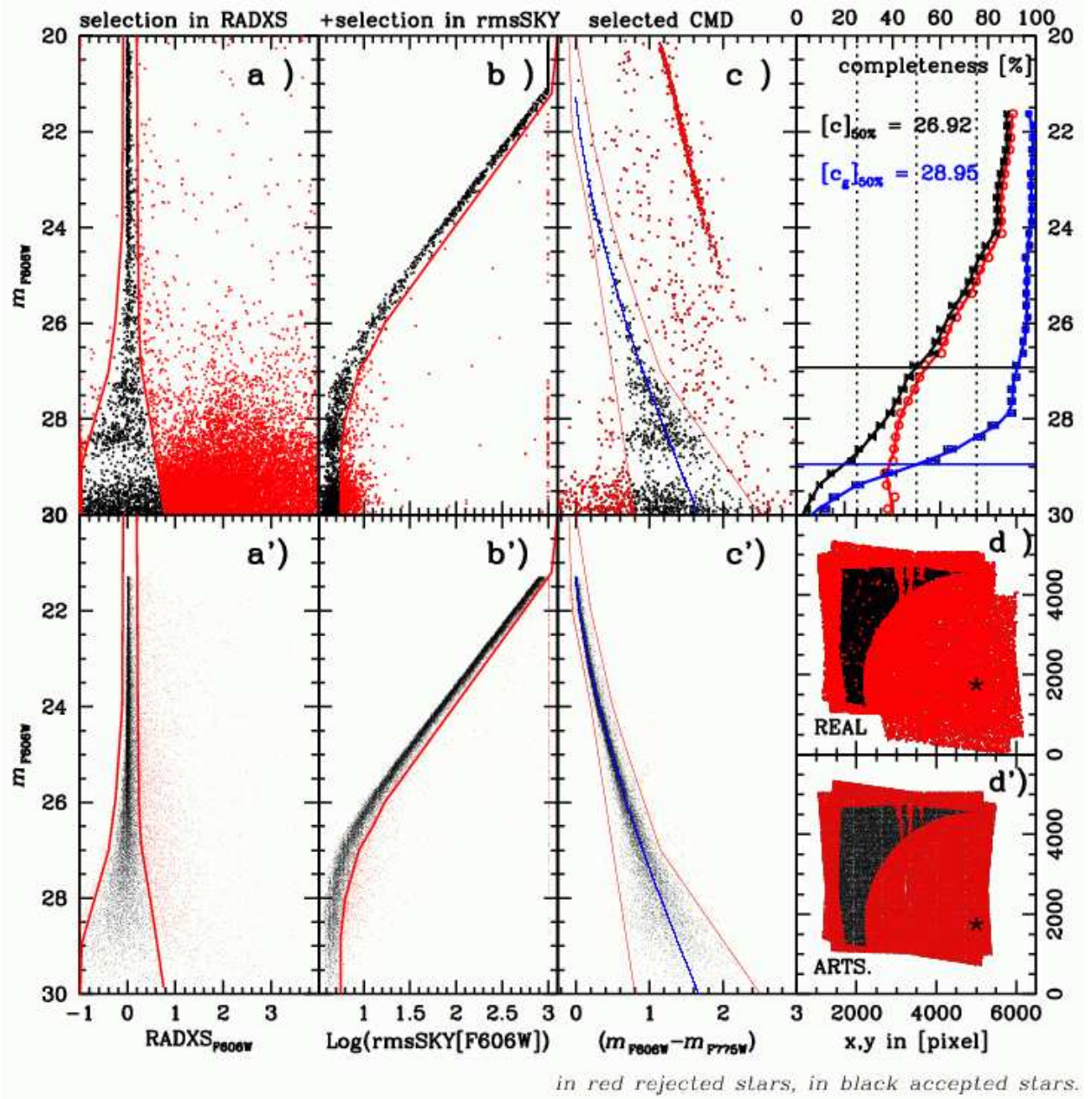


Fig. 5.— As in Figure 4, but selecting only those objects which are at least 140'' from the assumed position for the cluster center (marked with a  $\star$ ) in panels d) and d').

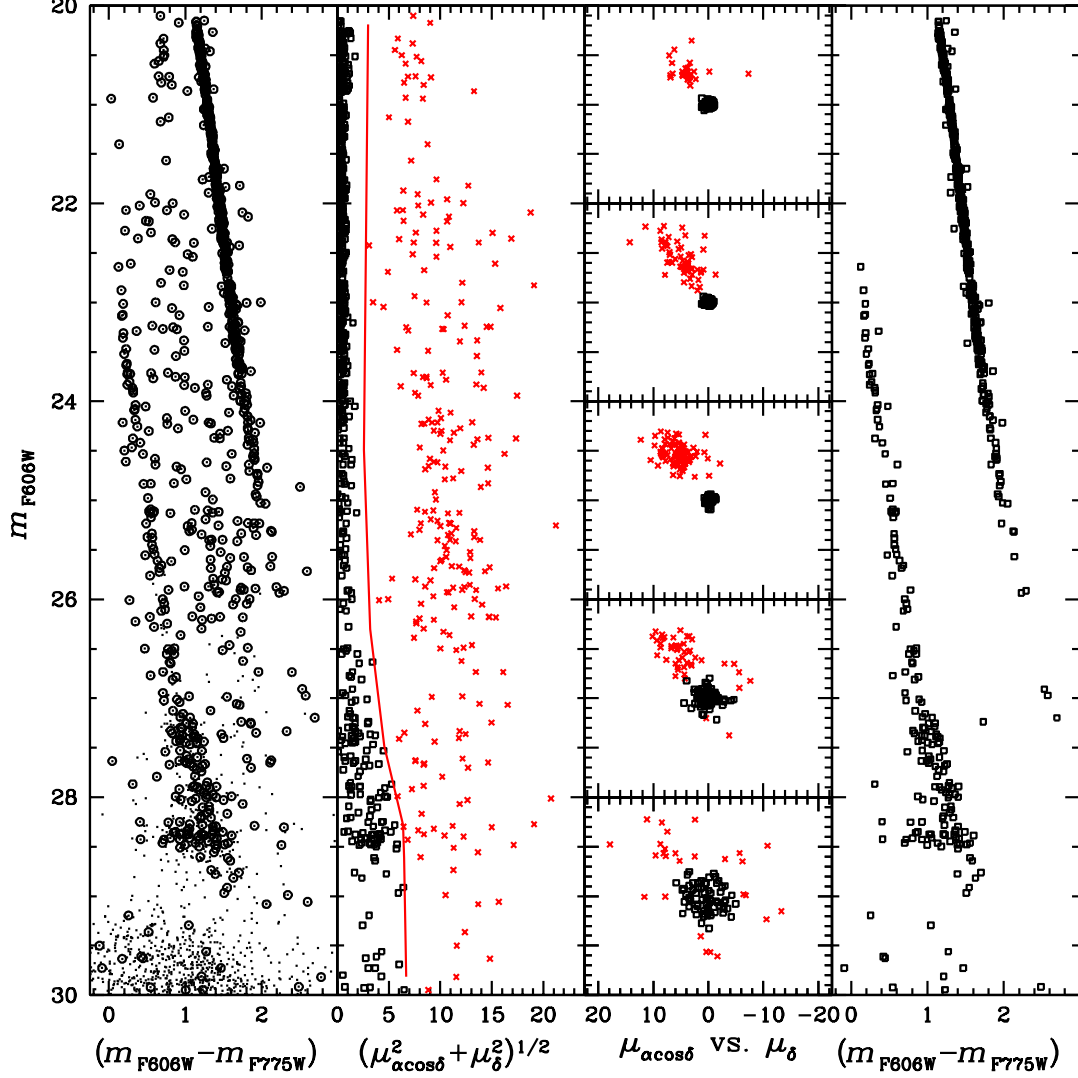


Fig. 6.— *(Left)*: Color-magnitude diagram for all stars in panel *c*) of Fig. 5. Small dots are all the stars, circles highlights the stars for which it was possible to measure a position in both epochs. *(Second panel from left)*: Total proper motion, in  $\text{mas yr}^{-1}$  relative to the mean proper motion of the cluster. Errors increase towards fainter magnitudes. The line was drawn in order to isolate the objects that have member-like motions (squares); red crosses show objects that we consider non-members. *(Third panel from left)*: Vector point diagrams for five different magnitude intervals indicated on the left-hand scale. *(Right)*: Proper motion-selected CMD (using criteria in second panel).

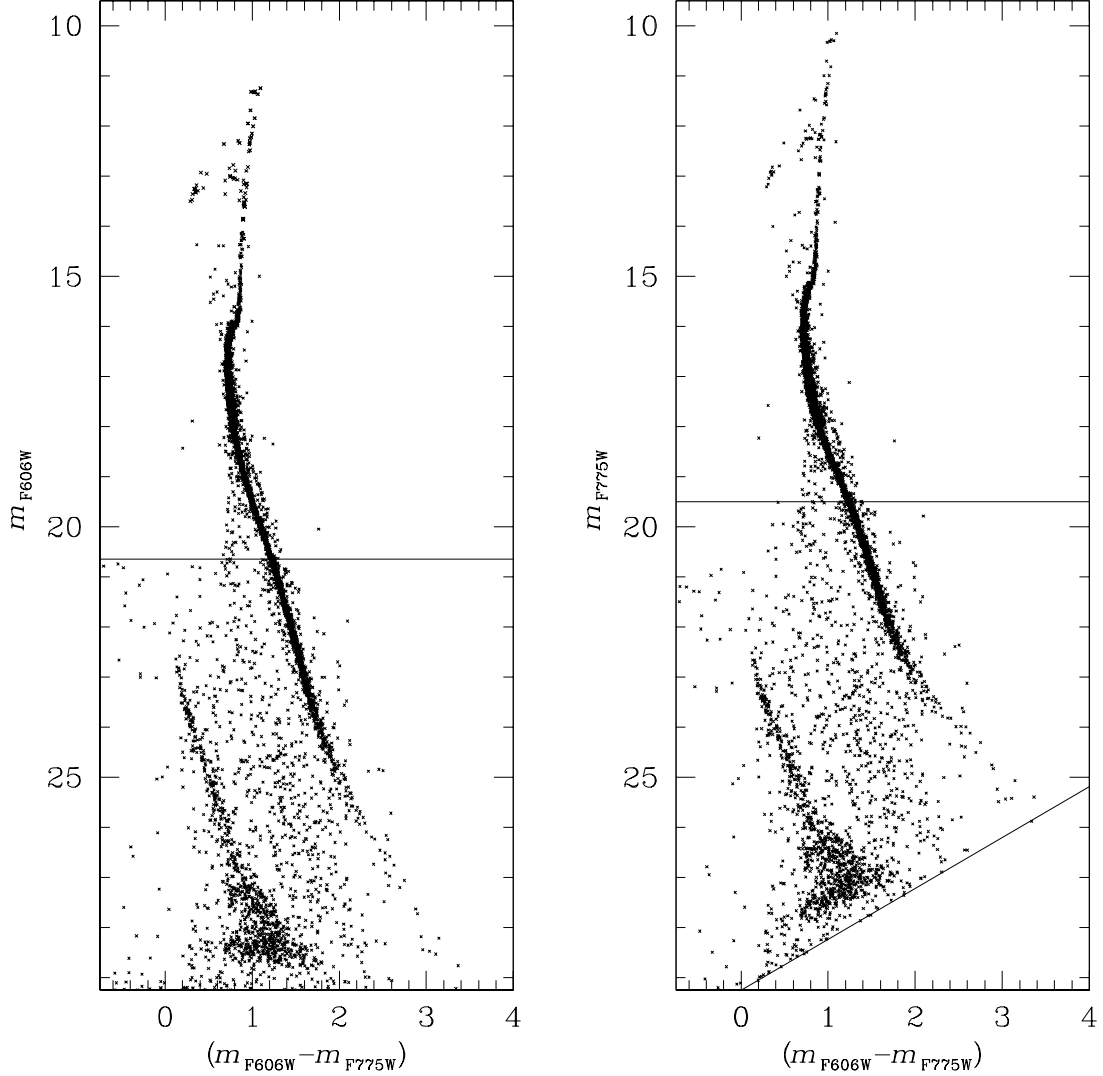


Fig. 7.— The objects in these CMDs (not selected for proper motions) span more than a factor  $10^7$  in luminosity. The bright stars were measured in the short exposures, then adjusted to the zero point of the deep exposures. The horizontal lines mark the saturation levels of images with exposure times of  $\sim 1200$  s. For deep photometry we show the stars in panel c) of Fig. 4. In the right-hand panel we show only the same objects that appear in left-panel. A diagonal line marks the location of the cut introduced by the faint  $m_{F606W}$  limit.

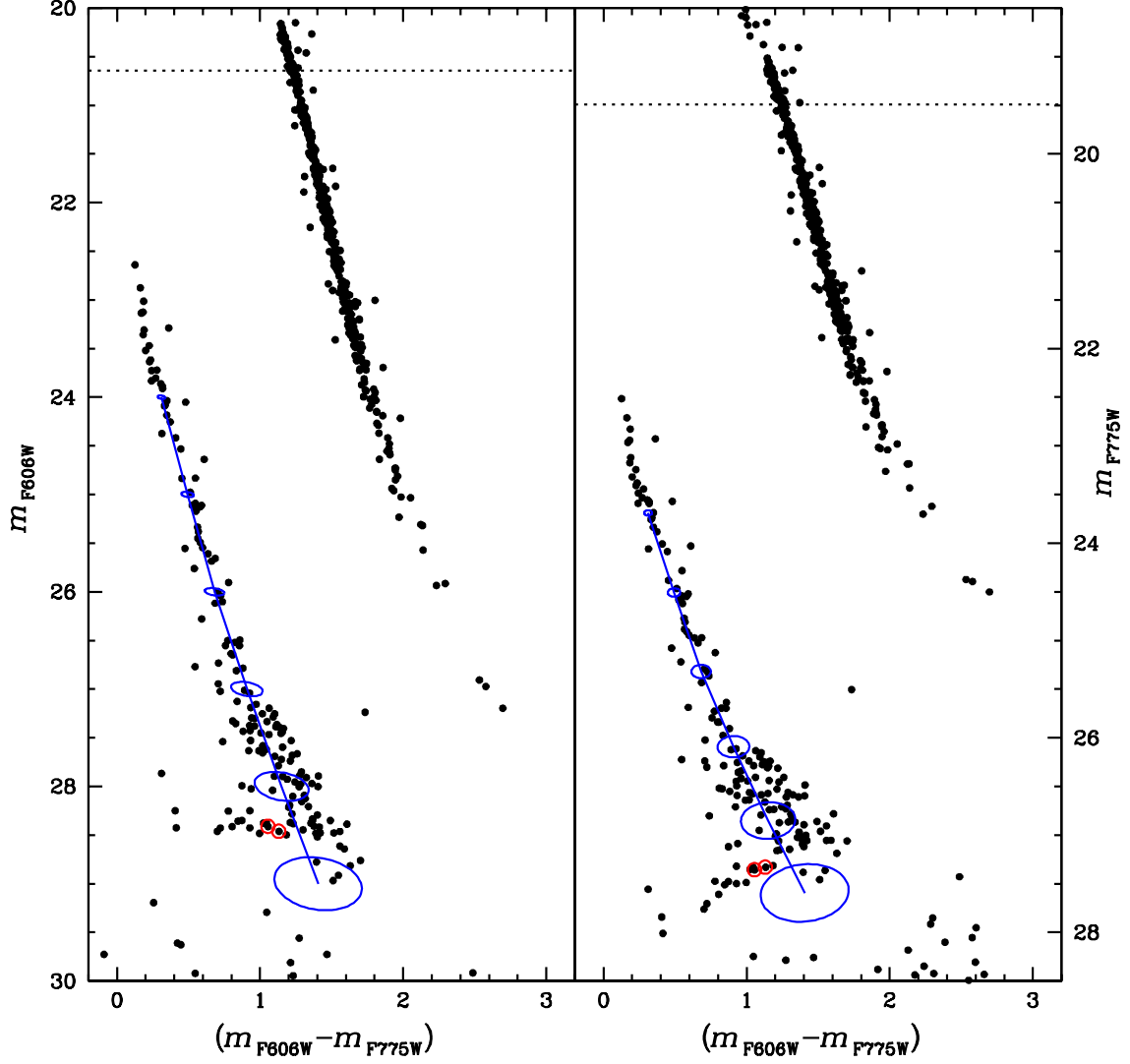


Fig. 8.— Decontaminated CMDs for a sub-sample of stars for which it was possible to estimate proper motions. Dotted lines indicate where saturations set in. Error ellipses along the WD fiducial line on each panel indicate the estimate of photometric rms errors along the WD CS. Two stars on the WD LF peak are highlighted by red open circles and shown in the stack images, in Fig. 9.



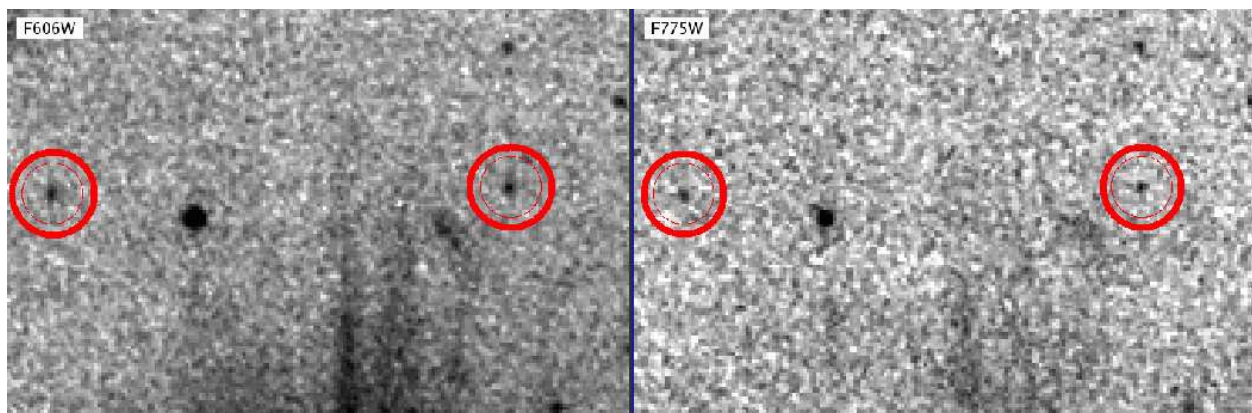


Fig. 9.— The two stars highlighted with red circles on the stacked images in filter F606W (left) and F775W (right) are stars that lie at the faint end of the WD CS. These two objects are real and relatively easy to measure [ $(m_{\text{F606W}} - m_{\text{F775W}}, m_{\text{F606W}}) = (1.13, 28.46)$  for the star on the left, and  $(1.06, 28.41)$  for the one on the right].

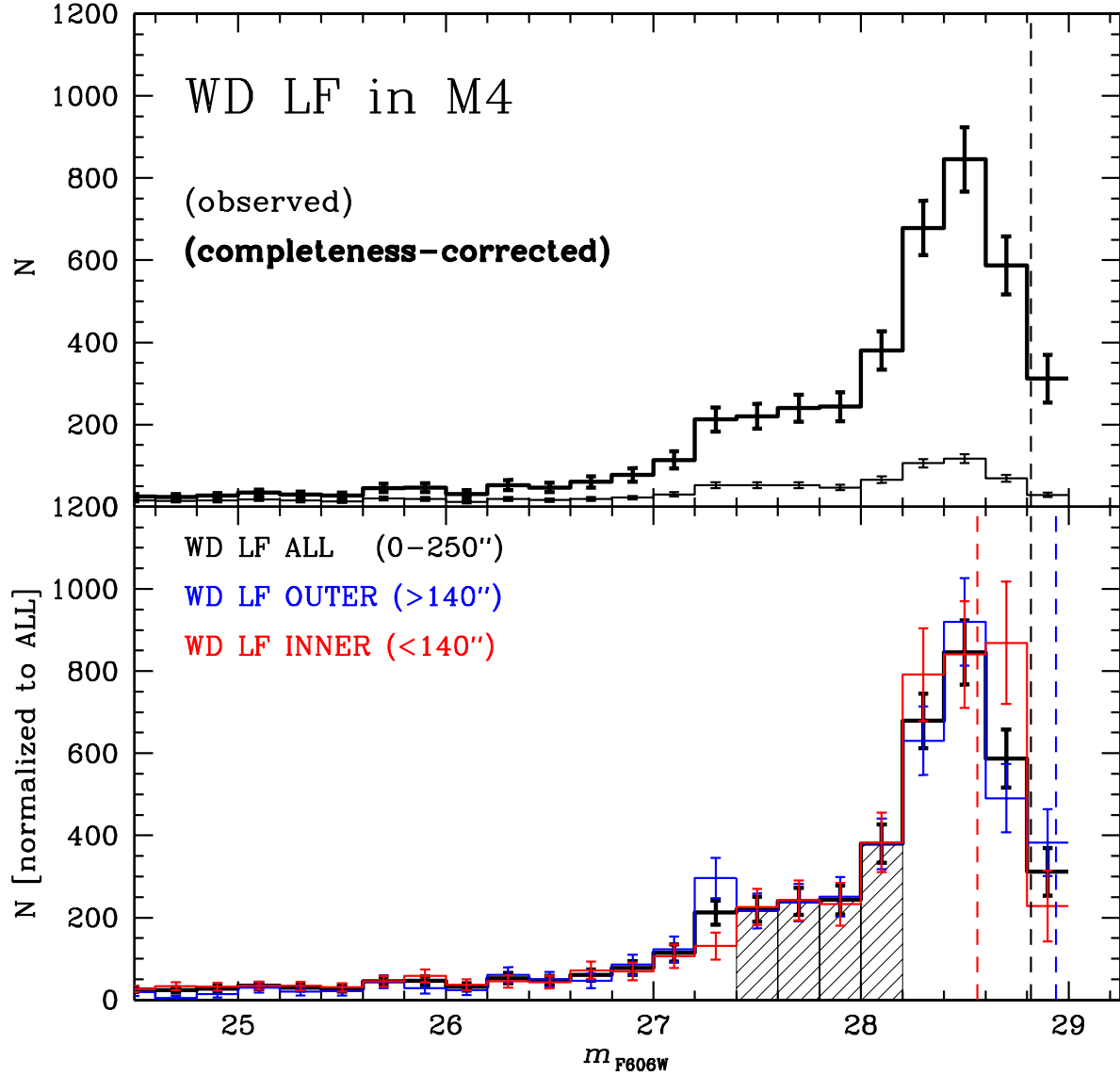


Fig. 10.— (*Top* :) White dwarf luminosity function in our field, as observed (thin line), and after correction for completeness (thick line). The vertical dashed line indicates the level of  $c_g = 50\%$ , below which our completeness becomes unreliable. (*Bottom* :) Completeness-corrected LF for WDs within  $140''$  of the cluster center (INNER, in red), and for WDs at larger distances (OUTER, in blue), with the  $c_g = 50\%$ -completeness magnitude levels marked by vertical dashed lines of the corresponding color. The shaded bins of the histograms indicate where the normalization was done. Note that the  $c_g = 50\%$  level for OUTER reaches the faintest magnitudes, allowing us to follow the drop of the WD LF for almost two bins after the peak at  $m_{F606W} = 28.5$ . Note also that crowding seems to make the WD LF peak somewhat broader in the INNER sub-sample than in the OUTER.

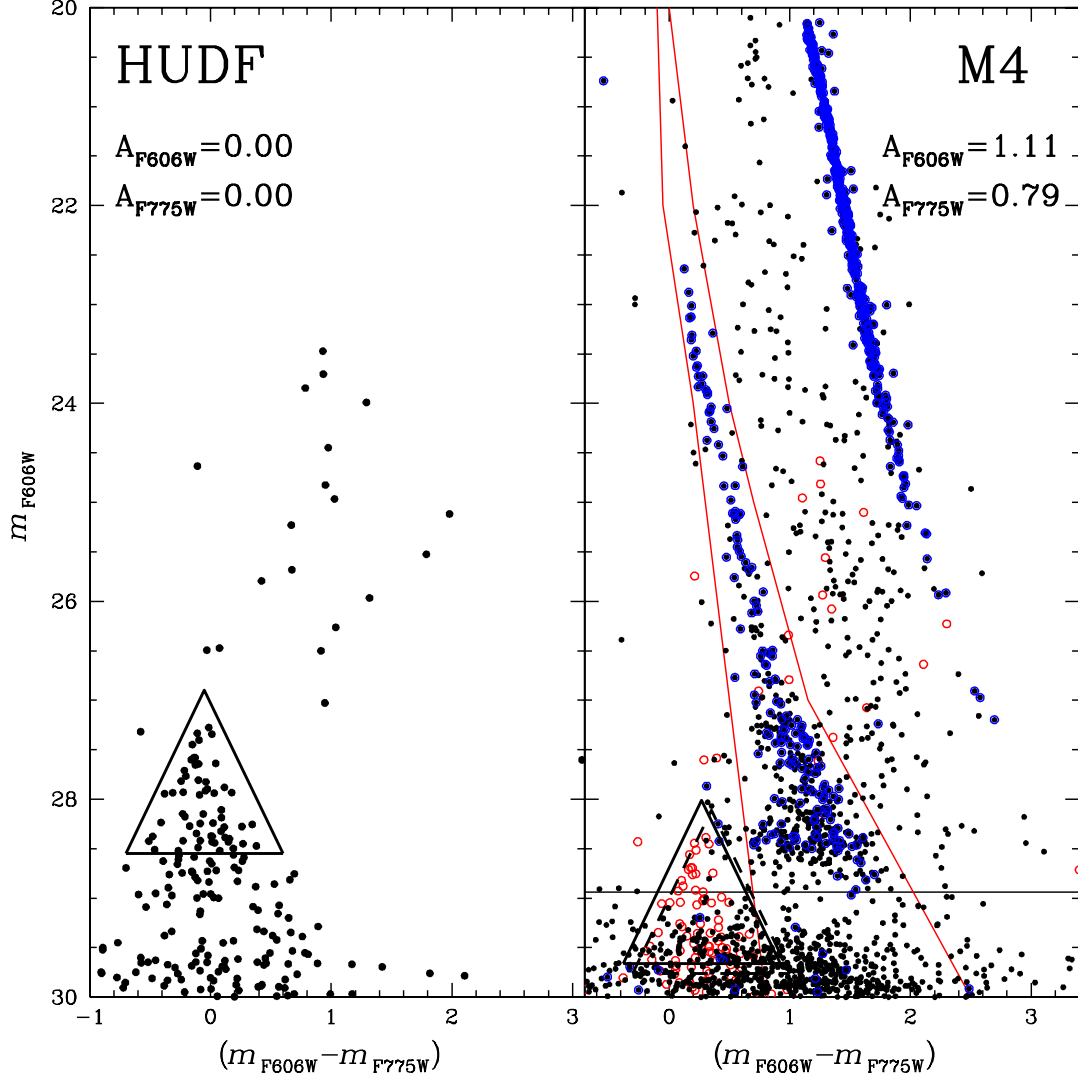


Fig. 11.— (*Left*) : CMD obtained from a subset of the Hubble Ultra Deep Field images, in its native observational plane. A triangle highlights the location of the point-like background sources in the magnitude range that might affect our WD counts. (*Right*) : Open red circles show HUDF objects shifted according to the estimated reddening in our M4 field. The triangle is also shifted according to the value of the extinction for cool objects, estimated using Table 3 in Bedin et al. (2005b). The dashed triangle has instead had extinction added for hot objects according to Table 4 in Bedin et al. (2005b). The two thin red lines delimit the region of what we consider a WD. The horizontal line marks the 50% completeness level of  $c_g$ . Black points mark objects in panel c) of Fig. 5, while the blue circles highlight the proper-motion selected sample of Fig. 6.

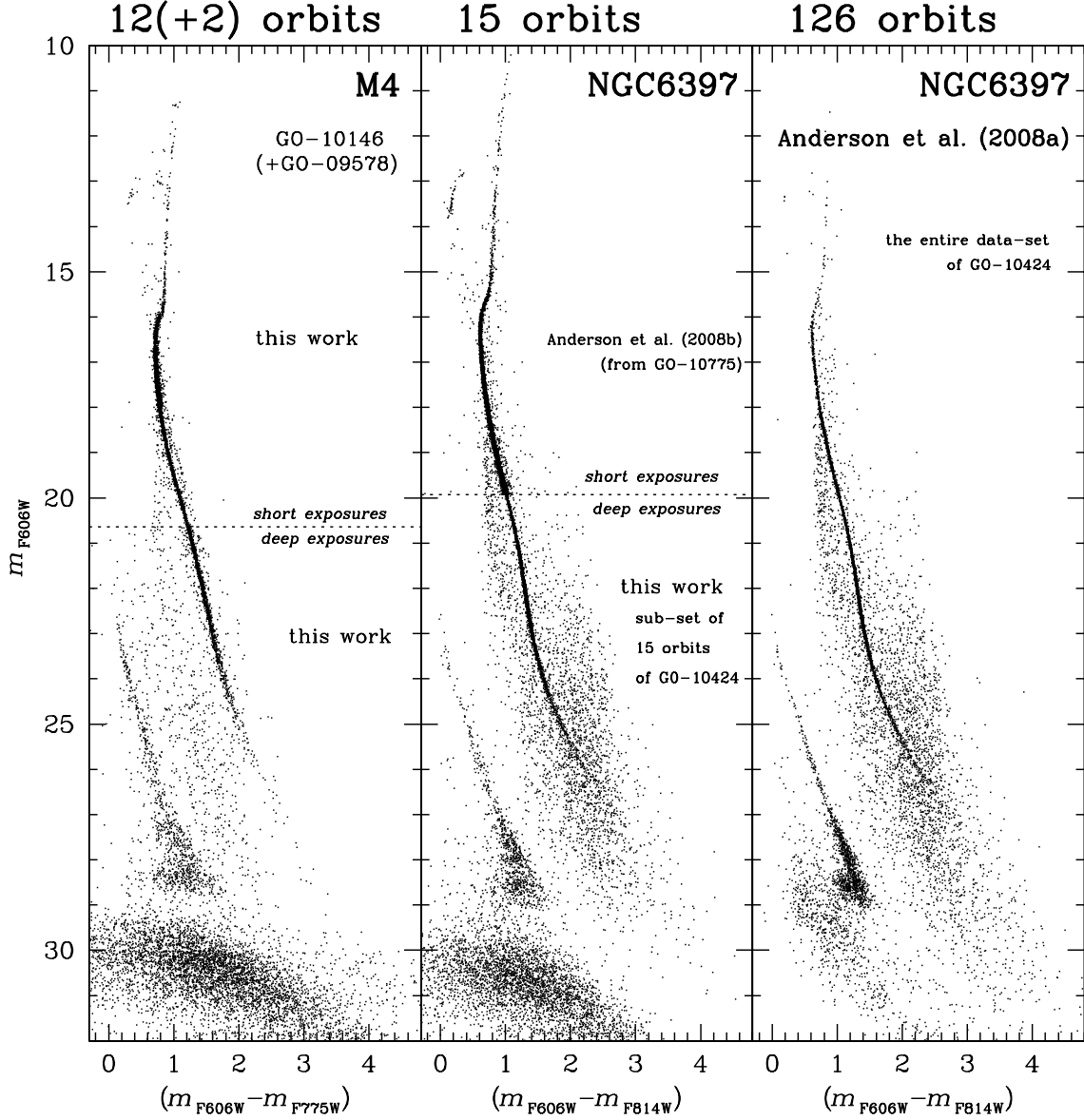


Fig. 12.— (*Left*) : CMD for M4 obtained combining our 12-orbit program with 2 orbits from the archive. Dotted lines indicate the onset of saturation for deep exposures. (*Middle*) : CMD for NGC 6397 using a subset of the GO-10424 images having the same total amount of exposure time for each filter of our M4 program. Photometry above saturation comes from a central field analyzed by Anderson et al. (2008b). (*Right*) : CMD for NGC 6397 obtained by Anderson et al. (2008a) using the entire 126-orbit data set.

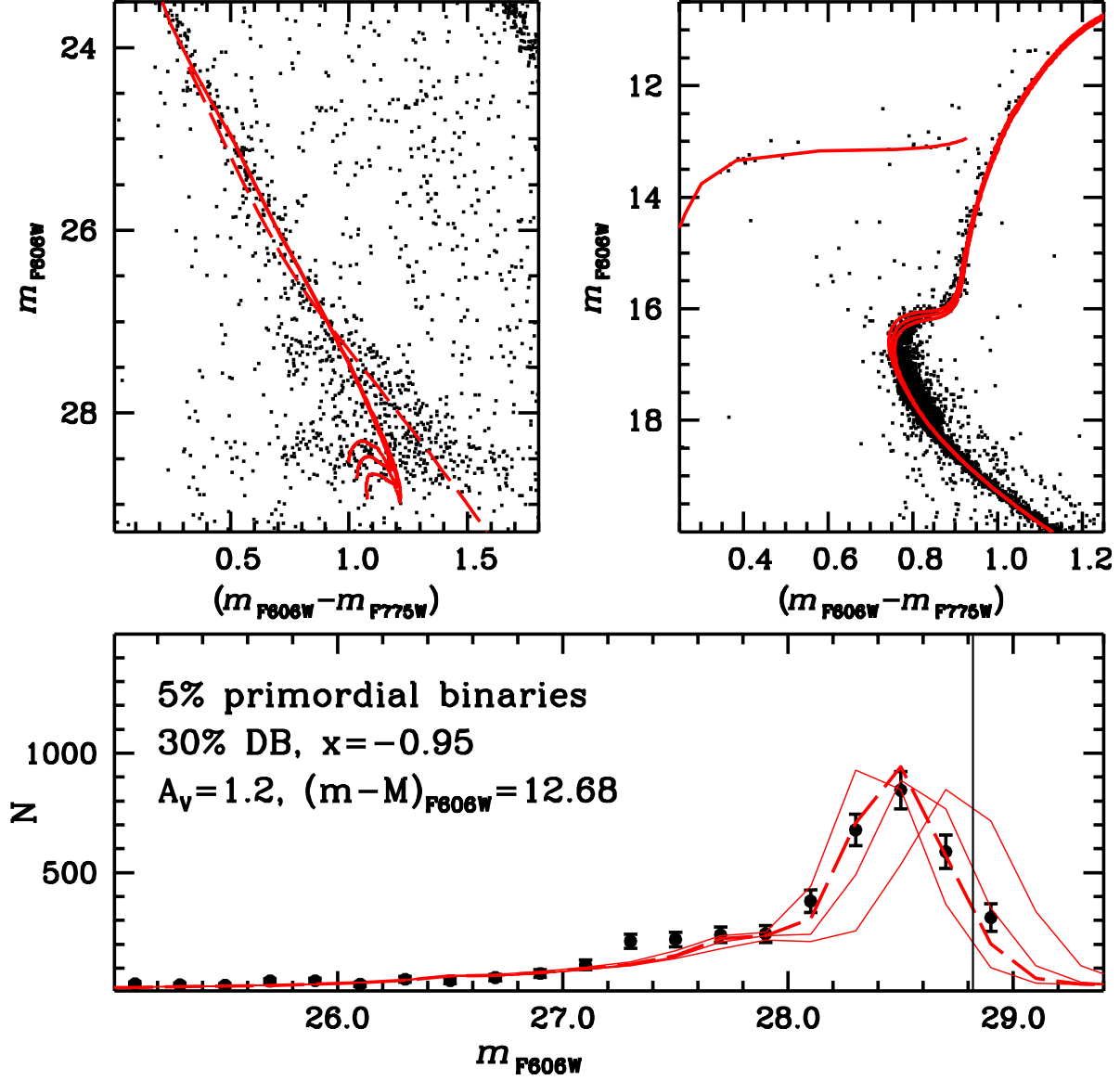


Fig. 13.— (*upper right panel*): Fit of theoretical isochrones to the cluster photometry, from the MS to the ZAHB, for ages of 11, 12 and 13 Gyr. (*upper left panel*): Similarly for WD isochrones; here solid lines denote DA models, dashed line DB models. The *lower panel* displays the fit of theoretical LFs for 11, 11.6 (dashed line), 12, and 13 Gyr to the observed star counts. The parameters of the theoretical LFs are also displayed. The isochrone fits employ the same extinction and apparent distance modulus as the LF fits.